# CHAPTER 2

# INTRODUCTION AND REVIEW

## 2.1. Langmuir Monolayers and Langmuir Films

## 2.1.1. General Review

Around the $18^{th}$ century BC, Babylonians used oil divination to predict death, illness, recovery, etc.[27] The predictions from the oil divination were based on the observation of the spreading behavior of oil on a water surface. These earliest observations of spreading oil films on a water surface were recorded on clay tablets by the Babylonians. In 1774, the concept of spread monolayers was first introduced to the scientific arena by Benjamin Franklin with his famous Clapham pond experiment.[28] In his experiments, he studied the effects of oil films on vibrations at the air/water (A/W) interface. His experiments stimulated further investigations mainly in Germany.[29] About one-hundred years after Franklin's experiments, Lord Rayleigh demonstrated that the extended oil films formed at the A/W interface were one molecule thick and indicated that the thickness could be estimated by determining the area occupied by the film-forming molecules.[30] About the same time, Agnes Pockels, a German scientist, devised a simple apparatus, essentially the prototype of a Langmuir trough, and published the first surface pressure-area isotherm in Nature.[31] In the early 1900's, Irving Langmuir designed a number of new devices for measuring the pressures of spread monolayers, one such device was later named a Langmuir film balance, which is a technique that is still being used for monolayer research.[32, 33] Langmuir's experiments confirmed that the thickness of a monolayer is one molecule and the existence of short-range forces is the basis of well-ordered film

formation.[32]  In 1919, Katherine Blodgett successfully transferred fatty acid monolayers from a water surface to glass substrates.[34]  The transferred multilayer films are now called Langmuir-Blodgett (LB) films. These studies, along with contributions from other scientists, provide the foundations of monolayer studies and the subject of monolayer assemblies.

Langmuir monolayers are usually formed by insoluble amphiphilic materials, such as stearic acid, which has two distinct regions in one molecule: a hydrophilic headgroup to anchor the molecule on an aqueous surface and a hydrophobic tails to keep the molecule from dissolving into the subphase.[33, 35, 36]  These well-spread amphiphilic molecules will rapidly cover the available surface area and arrange themselves at the A/W interface to minimize their free energy during compression.  The well-ordered surface layer thus formed at the A/W interface, with headgroups immersed in the water and hydrophobic tail pointed into the air, is called a Langmuir monolayer.[35]  Langmuir monolayers are uniform on a molecular scale.

In contrast, another commonly used term is Langmuir films, which describes both monolayer and multilayer films formed at the A/W interface.  In addition, the morphology of Langmuir films can be either homogeneous or heterogeneous.  The term Langmuir films can also be used to describe surface films formed by non-classical amphiphilic materials, molecules exhibiting surface activity but with heterogeneous surface morphology.  Langmuir films can sometimes be transferred onto solid substrates by the Langmuir-Blodgett (LB) or Langmuir-Schaeffer (LS) methods.[33, 36]  The transferred films are called LB-films or LS-films.

Many *in situ* methods were developed to investigate Langmuir films at the A/W interface, including Brewster angle microscopy,[37, 38] fluorescence recovery after photobleaching,[39-41] surface light scattering,[42-44] etc. The characterization methods developed for characterizing transferred LB-films or LS-films are even greater, such as atomic force microscopy (AFM), scanning electron microscopy (SEM), transmission electron microscopy (TEM), Fourier transform infrared spectroscopy (FTIR), ultraviolet-visible spectroscopy (UV-vis), etc. The range of film-forming materials has also been enlarged; not only covering the classical amphiphilic molecules, but also including the long chain substituted aromatic compounds, dyes, polymers, biological materials, porphyrins, fullerenes, inorganic-organic hybrid polymers, etc.[45-48]

## 2.1.2. Langmuir Monolayer Formation

Langmuir monolayers are only formed by certain types of molecules. Classical film-forming materials are small molecule amphiphiles, including phospholipids, and long alkyl-chain fatty acids, alcohols, and esters.[35, 36, 45] The molecular structures of these amphiphiles have a hydrophobic tail (long hydrocarbon chain) and a hydrophilic headgroup (polar group like –COOH and –OH). The hydrophilic headgroup tends to anchor the molecule on an aqueous surface and the hydrophobic tail prevents the molecule from dissolving into the subphase. The balance between these opposing forces affects an amphiphile's stability on the water surface, which determines the surface properties of any resulting Langmuir monolayer. Both synthetic polymers and some bio-macromolecules exhibiting surface activity are examples of non-classical film-forming materials. These materials can form insoluble layers at the A/W interface, which undergo less complicated phase transitions relative to fatty acids during dynamic compression.

Although some of these materials can spread spontaneously from bulk phases at the A/W interface, it is more common that most of these film-forming materials do not spread well by themselves and need to be dissolved into a spreading solvent. A spreading solvent shall be of high purity and completely spread film-forming molecules on the A/W interface to avoid the introduction of surface-active contaminants and defects into the film.[35, 36, 45, 46] In addition, the spreading solvent must be volatile and evaporate within a reasonably short period of time. Extremely volatile solvents can result in large errors with respect to spreading solution concentration. In general, experiments performed at or close to room temperature commonly use spreading solvents with boiling points in the range of 40 - 80 $^{\circ}$C. Furthermore, the spreading solvent should be insoluble in water. The more soluble the spreading solvent, the more the spreading solvent that accumulates in the subphase. Spreading solvent accumulation in the subphase can alter the surface properties of the subphase and monolayer formation. Considering all requirements for selecting a spreading solvent, chloroform has been the most commonly used volatile organic solvent with relatively low solubility in water and a moderate boiling point. In particular, chloroform solutions can easily spread over the water surface in comparison to other organic spreading solvents.
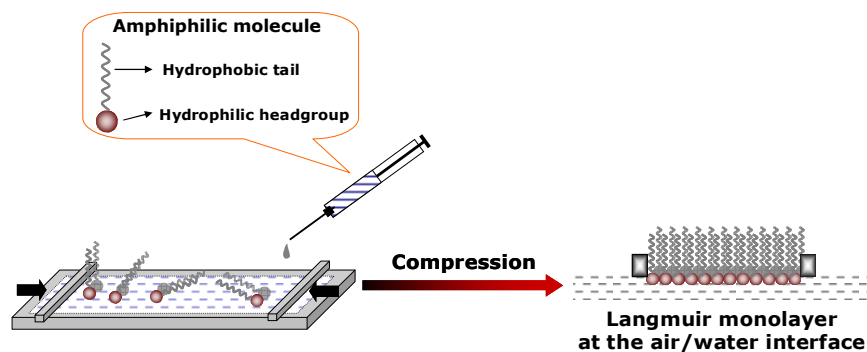
**Figure 2.1.** Formation of Langmuir monolayers

Once the spreading solvent is selected, the film-forming materials prepared as dilute solutions can be spread on the pure water subphase as depicted in Figure 2.1. The spreading solution spreads over the entire water surface and the film-forming molecules are deposited on the surface as the spreading solvent evaporates. The monolayers thus formed will undergo different phase transitions with various molecular chain conformations upon compression of the film.[35]

### 2.1.3. Surface Pressure (Π)-Area per Molecule (A) Isotherms

The line force acting on insoluble molecules at the A/W interface is referred to as the surface tension, $\gamma$ , a force per unit length, which can also be thought of as an energy per unit area, reflecting the tendency of liquids to reduce their surface area. Surface tension acts on the surface along a tangential direction. If the film-forming materials at the A/W interface are spread to dilute enough surface concentrations, the interactions between molecules are negligible and only small surface tension changes are observed. Upon compression of the film, the molecules will exert strong short-range forces on each other in the closely packed states. This condition is analogous to the intermolecular interactions

observed at higher pressure in bulk liquids and solids.  At equilibrium, the surface tension

at the A/W interface can be expressed as[35]

$$\gamma = \left(\frac{\partial F}{\partial A}\right)_{T,V,n_i} = \left(\frac{\partial G}{\partial A}\right)_{T,P,n_i} \tag{2-1}$$

T, P, V, and $n_i$ have their usual meanings of temperature, pressure, volume, and moles of

species i, respectively.  F and G are the Helmholz and Gibbs free energies, respectively,

and A is the interfacial area.

In studies of Langmuir monolayers or Langmuir films, the two-dimensional (2D)

analog of the three-dimensional (3D) P is called surface pressure, $\Pi$.  $\Pi$ is defined as the

difference between the surface tension of a film covered surface, $\gamma$, and a pure liquid

subphase, $\gamma_0$, as done in Eq. 2-2:

$$\Pi = \gamma_0 - \gamma \tag{2-2}$$

The surface pressure is also a force per unit length, while bulk pressure has units of

force per unit area.  Thus, the correspondence between $\Pi$ and P values is that the surface

pressure will become bulk pressure if another dimension, thickness of the monolayer

films, is considered and boundary stresses are ignored as seen in Eq. 2-3.

$$P(mN \bullet m^{-2}) = \frac{\Pi(mN \bullet m^{-1})}{thickness(m)} \tag{2-3}$$

Pure water has a surface tension of about 73 mN·m$^{-1}$, which is relatively high

compared to organic liquids because of strong hydrogen bonding between water

molecules.[35]   The presence of a molecular film at the A/W interface will decrease the

surface tension of pure water by decreasing the surface energy of water molecules because

of interactions between water and the amphiphiles. The surface tension can be measured by the Wilhelmy plate technique as depicted in Figure 2.2.
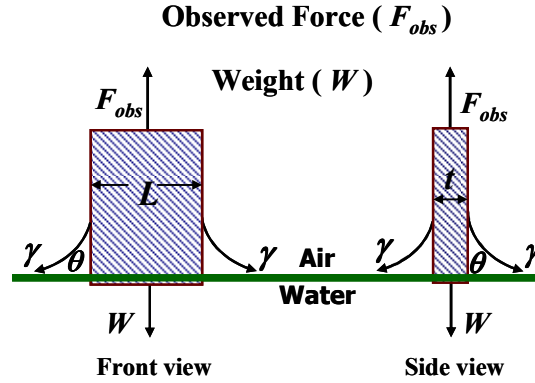


**Figure 2.2.** Measurement of surface pressure, $\Pi$, at the A/W interface.

The surface tension and surface pressure can be calculated from the following equations:

$$\gamma = \frac{F_{obs,film} - W}{2(L+t)\cos\theta} \tag{2-4}$$

$$\Pi = \gamma_0 - \gamma = \frac{F_{obs,0} - F_{obs,film}}{2(L+t)\cos\theta} \tag{2-5}$$

where $F_{obs,\,film}$ is the force measured by the Wilhelmy plate, W is the gravitational force, L is the length of plate, t is the thickness of the plate, which is usually negligible compared to L ($t \sim 0$) and $\theta$ is the contact angle between the liquid subphase and the plate as shown in Figure 2.2. Eqs. 2-4 and 2-5 assume the buoyant force is negligible. When filter paper is used as the Wilhelmy plate, it can be perfectly wetted with water ($\theta \sim 0$). Thus, Eq. 2-5 simplifies to:

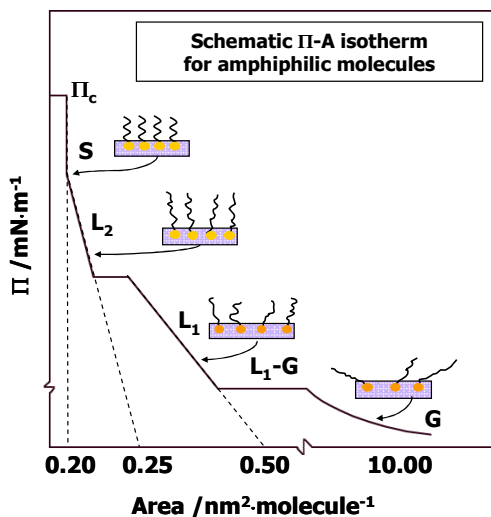$$\Pi = \gamma_0 - \gamma = \frac{F_{obs,0} - F_{obs,film}}{2L} \tag{2-6}$$

**Figure 2.3.** A schematic $\Pi$-A isotherm for an amphiphilic molecule. G: gas phase; $L_1$-G: coexisting liquid expanded and gas phases; $L_1$: liquid expanded phase; $L_2$: liquid condensed phase; S: solid phase; and $\Pi_c$: collapse pressure.

The most important quantitative characterization of a Langmuir monolayer at the A/W interface is its $\Pi$-A isotherm, which reflects changes in surface pressure upon compression or expansion of the films and is the 2D analog of a P-V diagram.[35, 36, 45, 46] Figure 2.3 is a schematic $\Pi$-A isotherm for traditional amphiphiles. Langmuir monolayers of traditional amphiphiles undergo phase transitions upon compression at the A/W interface and form phases that have similarities to gas, liquid, and solid phases in 3D. At very low surface concentrations, the 2D gas phase (G) is formed, which is comparable to a 3D gas phase as seen in Figure 2.4. At the A/W interface, the non-interacting molecules are randomly arranged in this regime. As the monolayers are compressed further, liquid-gas coexistent phases (L-G) can form as molecules become closer to each other and $\Pi$ increases. Upon further compression, molecules exist as a

liquid phase (L).  For some molecules, the liquid phase can be separated into a liquid-expanded phase ($L_1$ or LE) and a liquid condensed phase ($L_2$ or LC).  The formation of liquid-like monolayer phases in traditional lipids, such as fatty acids, is related to the chain length and packing of the hydrophobic tail.  Thus, the $L_1$ phase may not be observed for some molecules.  Likewise, some molecules, e.g. oleic acid, may only exhibit a $L_2$ phase.  The molecular surface density of the $L_1$ phase is smaller than the $L_2$ phase, which corresponds most closely to a 3D liquid; hence the compressibility of the film in the liquid-expanded phase is much greater than that of a 3D liquid.[35]
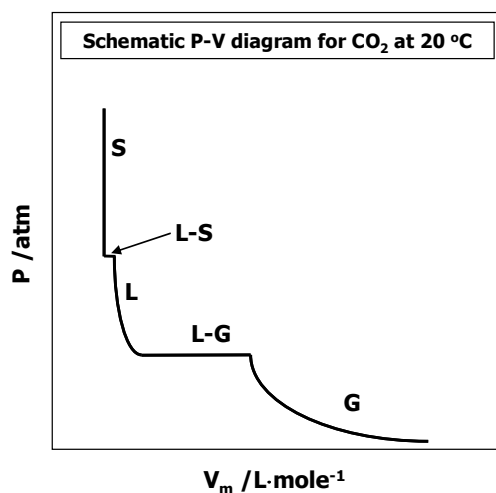


**Figure 2.4.** A schematic P-V diagram for $CO_2$ at 20 $^\circ$C. G: gas phase; L-G: liquid-gas coexistent phases; L: liquid phase; L-S: liquid-solid coexistent phases, and S: solid phase.

2D condensed monolayer

Monolayer collapse

"trilayer"          "bilayer"

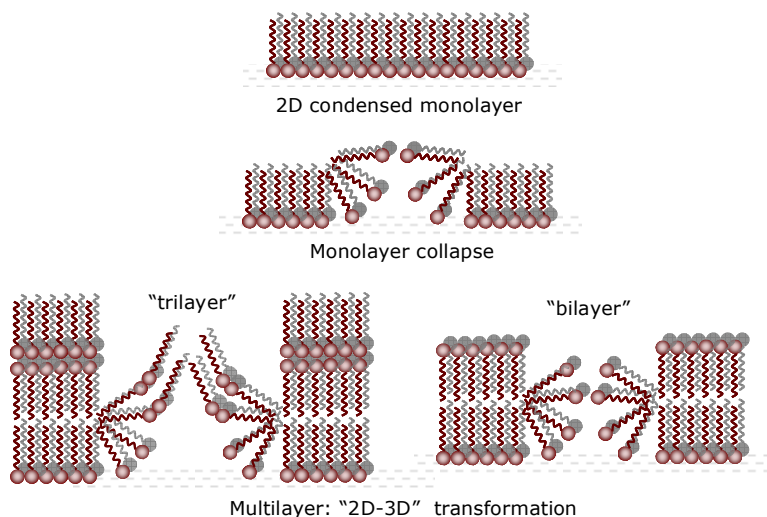Multilayer: "2D-3D" transformation

**Figure 2.5.** Schematic diagram of film collapse.

Upon the formation of the liquid condensed phase ($L_2$), the close packing of molecules restricts the molecular motion enough to only allow rotation.  Furthermore, molecules in the $L_2$-phase may take on tilted and/or untilted orientations.  Hence there are a number of different possible phases that can be differentiated through X-ray diffraction.[49, 50]  If a film forms a solid phase (S), the molecules are highly ordered and strong interactions exist between molecules.  The surface pressure corresponding to the collapse of the monolayer is called the "collapse pressure" ($\Pi_c$), where the compressibility of the monolayer approaches infinity.  The value of $\Pi_c$ indicates the limit of the stability for a two dimensional condensed monolayer.  After the collapse point, molecules can not maintain their ordered "2D" arrangement and begin to form multilayers as depicted in Figure 2.5 to dissipate the increased energy compression provides to the system.  However, for soluble surfactants like poly(ethylene oxide) (PEO), the monolayer is only stable below some critical surface concentration.[51]  At higher surface concentrations, PEO will be squeezed into the subphase, forming a thicker water swollen PEO layer with

increasing surface concentration, while the "surface" concentration of the uppermost layer remains almost constant.  The lowest molecular weight (MW) of PEO to form stable monolayers at the A/W interface is ~18 kg·mol$^{-1}$.  For PEO, the $\prod_C$ increases slightly with MW.  However, in the MW range from 145 to 996 kg·mol$^{-1}$, the collapse pressure, 10.2 mN·m$^{-1}$, is MW independent.[52]

   As the 2D Π-A isotherm is the surface analog to a 3D P-V isotherm, other physical properties in 2D monolayer systems can also have their counterparts in 3D bulk systems.[35]  One of examples is the rheological behavior of surface films, which is very useful in the discussion of Langmuir monolayers.  For 3D bulk systems, the bulk modulus, K, is given by

$$K = -V\left(\frac{\partial P}{\partial V}\right)_T \tag{2-7}$$

The corresponding 2D analog to the bulk modulus is the 2D lateral modulus, $\varepsilon_s$ , also called the static dilational elasticity.  $\varepsilon_s$ can be deduced from a Π-A isotherm as shown in Eq. 2-8:

$$\varepsilon_S = -A\left(\frac{\partial \Pi}{\partial A}\right)_T \tag{2-8}$$

The static dilational elasticity is related to the lateral compressibility of the monolayer, κ. The compressibility of monolayer can be defined as:

$$\kappa = -\frac{1}{A}\left(\frac{\partial A}{\partial \Pi}\right)_T \tag{2-9}$$

**2.1.4. Phase Transitions in Polymer Monolayers**

In the past decade, Brewster angle microscopy (BAM) has become one of the most effective methods for directly visualizing *in situ* morphologies of "2D" condensed phases of monolayers at the A/W interface through differences in refractive index between G, LE, LC, or solid phases at the A/W interface.[37, 38] These "2D" structures of classical amphiphilic molecules have been well studied and demonstrate an interesting variety of shapes and sizes, such as dendrites, fractal-like structures, and circular plates.[53-55] However, the "2D" phase diagram for polymers is much simpler as normally only the gas phase, one liquid phase, and a collapsed state have ever been observed as depicted in Figure 2.6.[56] One notable exception is poly(L-lactic acid), which has recently shown to exhibit a molar mass dependent LE/LC phase coexistence.[57, 58] The liquid-like polymer monolayer exists in an analogous state to the semi-dilute region of polymer solutions. $\Gamma^*$ is the overlap concentration from the dilute to semi-dilute region. When surface concentration $\Gamma = 1/A$ is below $\Gamma^*$, monolayers show gas-like behavior. For dilute enough $\Gamma$, non-interacting systems are observed, leading to molar mass dependent isotherms in accord with the ideal gas law.[56, 59, 60] With increasing $\Gamma$, intermolecular interactions become important and real gas behavior is observed.[56, 59, 60] As $\Gamma^*$ is approached, the "2D" coiled polymer molecules start to touch each other as depicted in Figure 2.7. Upon further compression, intramolecular interactions take on a critical role. Thus, within the semi-dilute region, the isotherms are no longer dependent on molar mass. Unlike 3D systems, polymer chain entanglements are not a critical factor during this process. With further compression, the liquid-like monolayer will ultimately undergo a "2D"-3D transformation at the collapse point.[56] The collapse states of polymer

monolayers show interesting variability according to the characteristics of their chain structures.
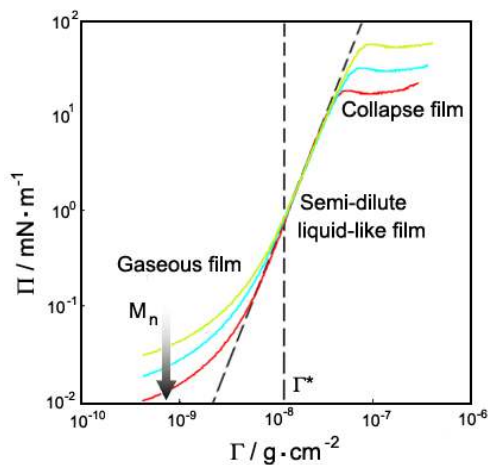


**Figure 2.6.** Schematic depiction of $\Pi$-$\Gamma$ isotherms for monolayers of a polymer. The isotherms indicate that a gas-like state, a semi-dilute liquid-like state, and a collapsed state exist for polymer monolayers. $M_n$ is the number average molar mass and $\Gamma^*$ is the overlap concentration.[56]
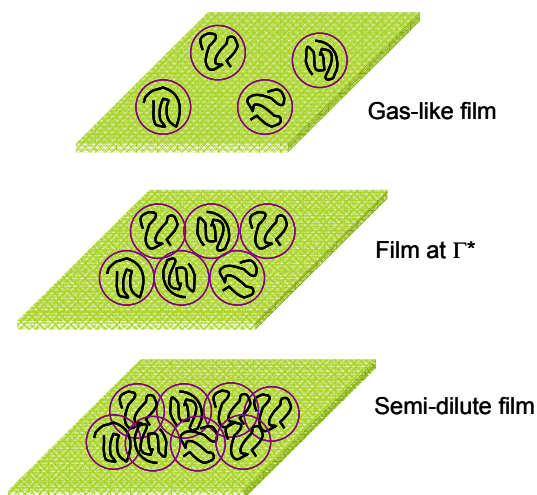


**Figure 2.7.** Schematic depiction of chain conformations of random coil polymers at the A/W interface.
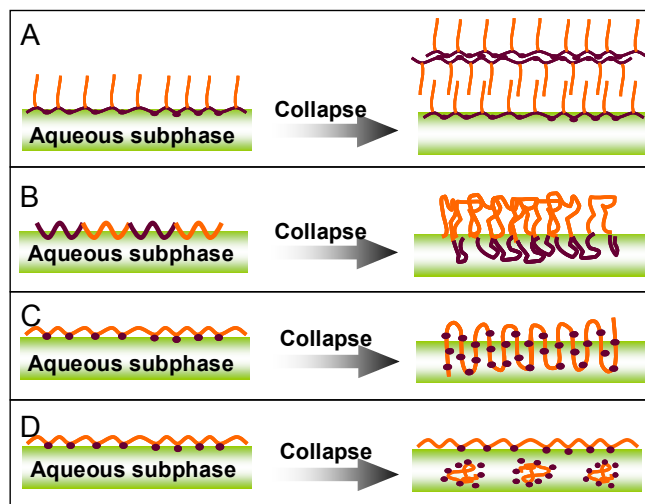
**Figure 2.8.** Schematic depiction of collapsed states of polymeric monolayers.[56] (A) Collapsed state and multilayer formation of comb-like polymers with strongly hydrophobic side chains; (B) Collapsed state of amphiphilic diblock polymers with hydrophilic chains squeezed into the subphase; (C) Folded loop structures formed during monolayer collapse of polymers having intermediate solubility; and (D) "Collapsed" state for monolayers where chains can desorb from the interface.

Figure 2.8A depicts the collapsed state and multilayer formation for comb-like polymers with strongly hydrophobic side chains. Collapse transitions in polymer monolayers are similar to small molecule amphiphiles. The collapsed state of amphiphilic diblock copolymers is depicted in Figure 2.8B, where the hydrophilic blocks are squeezed into the subphase. Thus, both mushroom and brush conformations are possible. If amphiphilic polymers are linear, flexible, and have an intermediate solubility, the polymer chains can form looped structures as seen in Figure 2.8C. Figure 2.8D corresponds to the collapsed state of monolayers formed by soluble polymers like

PEO. Upon compression past the collapse point, the polymer chains are squeezed into the subphase. "2D" to 3D transformations corresponding to the monolayer collapse become extremely important as far as polymer monolayers are concerned. The aim of this thesis is to present recent results for PCL crystallization in PCL or PCL-based blend monolayers. For the PCL system, the "2D"-3D transformation around the collapse point is similar to the process depicted in Figure 2.8C. Although, previous studies of collapsed states are mainly focused on small molecule amphiphiles, the proposed theories might be useful for polymer systems. Thus in the following sections, "2D"-3D transformations and an associated theory will be introduced. Some of previous studies on PCL monolayers will also be reviewed later in this chapter.

## 2.1.5. "2D" to 3D Transformations

During the compression of film-forming materials spread on the surface, $\Pi$ will increase and can even pass its maximum stable value, $\Pi_e$. $\Pi_e$ represents a limiting pressure above which relaxation phenomena occur when the monolayer is held at a constant surface pressure or a constant area per molecule.[61] Monolayer relaxation is characterized by either a decrease in area per molecule in an isobaric experiment or a drop in $\Pi$ if the trough area is held constant during the experiment. As long as the surface pressure is higher than $\Pi_e$, the monolayer lies in a supersaturated state or metastable state. Such supersaturated monolayers can exist over a wide surface pressure range below the dynamic collapse point.[53-55, 61-64] This state is analogous to bulk materials for which an equilibrium vapor pressure exists in the presence of its vapor. If this vapor pressure exceeds the equilibrium vapor pressure, materials in the gas state can deposit onto a solid surface as a liquid through a nucleation and growth process in a

supersaturated vapor. Nucleation and growth processes from supersaturated monolayers are analogous to nucleation and growth from supercooled or supersaturated bulk systems. For most long-chain insoluble monolayers, only the low $\Pi$ regime of a $\Pi$-A isotherm obtained by compression at a fixed rate corresponds to an "equilibrium state".

There have been numerous studies on the "2D" to 3D transitions of insoluble monolayers. "2D" to 3D transformations of monolayers frequently occur during "monolayer collapse"-a phase change related to the growth of a 3D phase from a close-packed "2D" monolayer in an over-compressed state. "Monolayer collapse" is usually observed as drop in $\Pi$ or a plateau region in a $\Pi$-A isotherm. The "2D" to 3D transition can occur within the plateau region at $\Pi_c$ such as behenic acid monolayers.[64] For some molecules, like stearic acid on an acidic subphase (pH 3.0) at 20 $^{\circ}$C, "2D"-3D transitions can start below $\Pi_c$, in the supersaturated monolayer. The 3D nuclei form at $\Pi_e < \Pi < \Pi_c$, and then grow and overlap within the plateau region.[64]

The $\Pi$ values and the shape of isotherms at the collapse point depend on the intermolecular interactions between amphiphiles, the compression rate, and the interactions between the molecules in the monolayer and the subphase.[64, 65] According to previous studies on the compression rate dependence of $\Pi_c$,[48(d), 65] the magnitude of $\Pi_c$ has been demonstrated to increase with compression rate. At higher compression rates, the ordered monolayers cannot relax faster than the rate of compression in a short period of time, thus the monolayers undergo a higher degree of supersaturation or undercooling and exhibit an increased dynamic value of $\Pi_c$. Consequently, the number of nuclei formed from a supersaturated monolayer increases with increasing compression rate. At a sufficiently high compression rate, the shape of the isotherm around the collapse point

can change from a "kink" to a "plateau" since it is impossible for monolayers to relax on such short experimental time scales.  Thus, at lower compression rates, the measured surface pressures are closer to the "equilibrium" values.  As mentioned above, the magnitude of $\Pi_c$ is an indication of monolayer stability.  Enhancements of monolayer stability will lead to an increase in the magnitude of $\Pi_c$.  Enhanced stability can be obtained by increasing the length of hydrophobic tails, introducing ionic or coordination interactions between amphiphiles and the subphase, etc.  Temperature is also a factor that can affect "2D" to 3D transformations due to its influence on intermolecular interactions and the hydrophilicity of the head groups.

**2.1.6. Nucleation and Growth Theory for Traditional Amphiphiles**

The supersaturation in monolayers upon compression can be considered as the driving force for the nucleation of "3D" phases from "2D" condensed monolayers.[66]  From a molecular point of view, the breaking and piling-up of "2D" condensed monolayers upon overcompression at or near $\Pi_c$ leads to the formation of 3D structures.  Nucleation-growth-collision theory developed by Vollhardt *et al.* has been used for theoretically describing the nucleation, growth, and overlapping of 3D centers in monolayers of traditional long-chain amphiphilic molecules.[67-71]  Two different models were developed that have the following features in common: (1) The total transformation rate is described as a convolution of the nucleation rate and the growth rate; and (2) The overlap of the growing centers in the succeeding stages of the process has also been considered.[67, 68, 70]
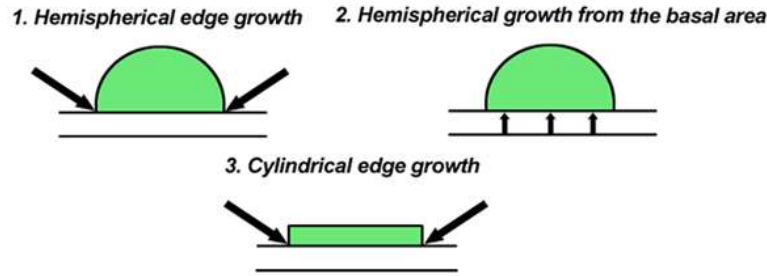
**Figure 2.9.** Geometries of 3D nucleation centers in monolayers.[68, 69]

The first model developed by Vollhardt *et al.* was an extension of the Avrami equation.[67-69] This model assumed homogeneous nucleation with a simple geometric shape for the 3D nuclei as seen in Figure 2.9.[68-69] The general expression for both instantaneous and progressive nucleation from this model is:

$$\frac{A_0 - A}{A_0 - A_\infty} = 1 - \exp\left(- K_x \left(t - t_i\right)^x\right) \tag{2-10}$$

where $A$ is the total area per molecule at time $t$, $A_0$ is the initial area per molecule, and $A_\infty$ is the area per molecule at $t \approx \infty$. An induction time, $t_i$, is introduced as a theoretical description of time dependent growth rates. A positive $t_i$ value indicates that the growth rate at early times is smaller than the normal value for the subsequent growth process, while a negative value suggests a higher growth rate at the start of nucleation. $K_x$ is an overall transformation rate constant that encompasses the nucleation rate, $k_n$, and growth rate, $k$. Instantaneous nucleation corresponds to large $k_n$ with $N \sim N_{max}$, while progressive nucleation is correlated to small $k_n$ with $dN/dt = k_n N_{max}$. $N$ is the number of nuclei at time $t$ and $N_{max}$ is the total number of potential nuclei forming sites at the A/W interface. Different nucleation models result in distinct $K_x$.[68] The exponent $x$ is specified according

to the different mechanisms of nucleation and growth and the geometries of the 3D nucleation centers (See Figure 2.9 and Table 2.1).[68, 69] Thus the nucleation mechanism can be inferred from the value of the exponent $x$ by fitting $A$ vs. $t$ data obtained from constant $\Pi$ experiments. Previously reported constant $\Pi$ studies of octadecanoic acid monolayers have clearly indicated that different nucleation mechanisms exist for different experimental conditions: (1) Area changes at $\Pi = 30$ mN·m$^{-1}$ and T = 30 $^{\circ}$C could be explained by instantaneous nucleation with hemispherical edge growth; and (2) For the case of $\Pi$ relaxation at $\Pi = 34$ mN·m$^{-1}$ and T = 20 $^{\circ}$C, progressive nucleation with hemispherical edge growth was observed.[68, 69]

**Table 2.1.** Exponents for different nucleation mechanisms and center geometries.[68, 69]

| Geometry of centers | Nucleation mechanism | Exponent $x$ |
|---|---|---|
| Hemispherical edge growth | Instantaneous | 3/2 |
| Hemispherical edge growth | Progressive | 5/2 |
| Hemispherical growth from basal areas | Instantaneous | 1 |
| Hemispherical growth from basal areas | Progressive | 4 |
| Cylindrical edge growth | Instantaneous | 2 |
| Cylindrical edge growth | Progressive | 3 |

Another generalized nucleation model assumed nucleation corresponding to the formation and growth of a lenticular nucleus. Two limiting cases: Instantaneous nucleation and progressive nucleation are also included in this model. The overlap of the growing centers and the effects of surface tension on the lenticular growth at the three phase contact (air/water/3D center) have been considered in this model.[70, 71] The expression derived for the generalized nucleation and growth model is given as:

$$\frac{A_0 - A}{A_0 - A_\infty} = 1 - \exp\left[- Ct^{3/2} F(k_n t)\right] \tag{2-11}$$

All constants corresponding to specific properties of the materials and the 3D centers were incorporated into the constant $C$. $k_n$ is the nucleation rate. Two limiting cases of nucleation are related to the boundary conditions of $F(k_n t)$,[71] which were mathematically described in Eqs. 2-12 through 2-15.

Instantaneous nucleation:

$$\lim_{k_n t \to \infty} F(k_n t) = 1 \tag{2-12}$$

$$\frac{A_0 - A}{A_0 - A_\infty} = 1 - \exp\left[- Ct^{3/2}\right] \tag{2-13}$$

Progressive nucleation:

$$\lim_{k_n t \to 0} \frac{F(k_n t)}{k_n t} = \frac{2}{5} \tag{2-14}$$

$$\frac{A_0 - A}{A_0 - A_\infty} = 1 - \exp\left[- \frac{2}{5} Ck_n t^{5/2}\right] \tag{2-15}$$

Unfortunately, previous studies found excellent agreement between the calculated and experimental A-$t$ curves of methyl stearate monolayers for both models, leading to an overall rate constant $(2/5)$ $Ck_n$ from model 2 that is vastly different from the $K_x$ value obtained from Eq. 2-10 for progressive nucleation.[69] This ambiguity could be related to the effects of the geometric shape of the 3D nucleation centers on the overall growth rates. At this time, there is still no method available for distinguishing between the two cases.

## 2.1.7. Previous Studies of Poly (ε-caprolactone) Monolayers at the Air/Water Interface

Polymeric monolayers and transferred LB-films have attracted greater attention than traditional amphiphiles since they have better thermal and mechanical stability. Poly (ε-caprolactone) (PCL) is one of several interesting linear flexible (homo-) polymers for monolayer studies. PCL based systems have attracted considerable interest for controlled-release drug delivery and as scaffolds for tissue engineering,[72-74] that require a fundamental understanding of PCL's degradation mechanisms and crystallization properties. PCL is degradable through base or enzyme catalyzed hydrolysis of its ester bonds. PCL degradation correlates to the molar mass, molecular orientation, chain packing, crystal surface, and crystallinity of the polymer.[75, 76] At the A/W interface, previous results indicate that PCL (16 kg·mol$^{-1}$) can form a "2D" close-packed monolayer with a collapse point around A ≈ 20 Å$^2$·monomer$^{-1}$. These Langmuir monolayers have been used to study base catalyzed PCL hydrolysis.[75] One of the advantages of the monolayer method is that the ester groups could be organized at the interface because of their hydrophilicity. Consequently, it is possible to realize the optimal conditions for hydrolysis or enzymatic degradation when all ester bonds are exposed to acidic or basic subphases with or without enzymes. Another advantage is the possibility of quantitative analysis of hydrolysis kinetics by monitoring the surface pressure change during the hydrolysis process at constant area or the decrease in area per monomer with time during isobaric measurements since the hydrolytic products, short fragments or monomers of PCL, are water-soluble. Previous results by Lee *et al.* demonstrate that base catalyzed hydrolysis of PCL blends with poly (L-lactic acid) (*l*-PLA) is faster than for either pure

component.[75]  This behavior may be related to the difference in crystallinity of PCL and its blends at the A/W interface.  Decreasing the order of a PCL monolayer through blending could assist the hydrolysis process by increasing the number of sites per unit area suitable for base catalyzed hydrolysis.[75]  In this thesis, BAM is used to study *in situ* morphologies of PCL crystals grown during compression (nucleation and growth: monolayer materials→3D solid) and melting during expansion (melting: 3D solid→"2D" phase) of a Langmuir film at the A/W interface.  These results are not only significant for future studies of the effect of crystallinity on enzymatic degradation, but also provide an interesting model system for studies of polymer crystallization in confined geometries at surfaces.

## 2.2. Binary Polymer Blends

### 2.2.1. Thermodynamics of Polymer Blends

Mixing two polymers yields either a miscible or immiscible blend.  If the mixing conditions and the chemical structures of the two components allow polymer chains to completely interpenetrate at a molecular level, the blend is miscible and homogeneous. However, most polymer blends are immiscible.[77]  The thermodynamic analysis of a binary polymer mixture starts with Eq. 2-16:

$$\Delta G_{mix} = -T\Delta S_m + \Delta H_m \qquad\qquad (2\text{-}16)$$

where $\Delta G_{mix}$ is the Gibbs free energy of mixing, $\Delta S_m$ is the entropy of mixing, and $\Delta H_m$ is the heat (or enthalpy) of mixing.  In polymeric systems, the high molar mass together with the intermolecular forces hinder molecular motion in the blends.  In addition, polymers usually have inherently high entropy in comparison to small molecules.  Thus, the change of $\Delta S_m$ for polymer blends becomes very small as the molar mass increases,

although $\Delta S_m$ always favors mixing for flexible coil polymers. The miscibility of polymer blends primarily depends on the change in heat of mixing (enthalpy of mixing), which is determined by intermolecular forces between the two components. Therefore, the mixing process is more favorable as attractive intermolecular interactions increase. In practical applications, it is sometimes possible to prepare miscible blends by replacing one of the two immiscible homopolymers by a copolymer of the two components to create a miscible system.[78]

Furthermore, the intermolecular interactions discussed here are short-ranged forces, including van der Waals interactions, hydrogen-bonding, dipole-dipole interactions, and electrostatic interactions. The interaction between two polymer components can be described through the Flory-Huggins interaction parameter, $\chi_{a,b}$ , as given by Eq. 2-17:[79]

$$\chi_{a,b} = \frac{Z[\varepsilon_{a,b} - (\varepsilon_{a,a} + \varepsilon_{b,b})/2]}{k_B T} \qquad (2\text{-}17)$$

where $\varepsilon_{a,b}$, $\varepsilon_{a,a}$, and $\varepsilon_{b,b}$ are the strength of interactions (negative values) between segments a-b, a-a, and b-b, respectively; and $Z$ is the coordination number. This interaction parameter takes into account the strength of interactions, the governing factor for determining the miscibility of polymer blends. A negative value of the interaction parameter arises from strong specific interactions between components a and b. Hence, the Gibbs free energy of mixing can be described by the Flory-Huggins equation:[79]

$$\Delta G_{mix} = RTn\left( \frac{\phi_a}{N_a} \ln \phi_a + \frac{\phi_b}{N_b} \ln \phi_b + \chi \phi_a \phi_b \right) \qquad (2\text{-}18)$$

where $\phi_a$ and $\phi_b$ are the volume fractions of polymers a and b, $N_a$ and $N_b$ are the degrees of polymerization for polymer a and b, R is gas constant, and n is the number of moles of

the reference unit (monomer). For a symmetric polymer mixture with equal degrees of polymerization for both polymers a and b, $N_a = N_b = N$. Furthermore, $n/N = n_a + n_b$, where $n_a$ and $n_b$ are the number of moles of polymer a and b, respectively. Thus, Flory-Huggins equation can be written as

$$\Delta G_{mix} \frac{N}{RTn} = \phi_a \ln \phi_a + \phi_b \ln \phi_b + \chi N \phi_a \phi_b \qquad (2\text{-}19)$$

The first two terms in Eq. 2-19 represent the entropy of mixing. The third term in Eq. 2-19 indicates the enthalpy of mixing (heat of mixing) arising from intermolecular interactions. It is worth noting that the miscibility of polymer blends depends on many factors such as temperature, composition, etc.[77, 79] There is almost no pair of completely miscible or immiscible polymers. The miscibility window can be either very broad or very narrow, depending on the chemical structures of polymers, their molar masses, their stereochemistry, etc.[77, 79] For binary polymer blends a critical point is observed when $\frac{\partial^2 \Delta G_{mix}}{\partial \phi_a^2} = \frac{\partial^3 \Delta G_{mix}}{\partial \phi_a^3} = 0$. The critical value of the interaction parameter, $\chi_c$, and the critical composition, $\phi_{a,c}$, are given by[80]

$$\chi_c = \frac{1}{2} \left( \frac{1}{\sqrt{N_a}} + \frac{1}{\sqrt{N_b}} \right)^2 \qquad (2\text{-}20)$$

$$\phi_{a,c} = \frac{\sqrt{N_b}}{\sqrt{N_a} + \sqrt{N_b}} \qquad (2\text{-}21)$$

The value of $\chi_c$ is very small and eventually approaches zero as the molar mass of the polymers becomes very large. In the limit of infinite molar mass, the polymers are completely immiscible for all positive values of $\chi$. For a symmetric binary polymer

blend, the critical value of ($N\chi_c$) is equal to 2, below which there is perfect miscibility for all compositions. Therefore, perfect compatibility is expected for blends with $\chi < \chi_c$ over the entire range of composition.  For $\chi > \chi_c$, the binary blend has a miscibility gap.  The dependence of $\chi$ on composition is usually negligible except in the limit where one component is very dilute in the blends ($\phi_a$ or $\phi_b \leq 0.15$).[77, 80] Furthermore, the temperature dependence of $\chi$ for polymer blends with only dispersive interactions is normally given as

$$\chi = A + \frac{B}{T} \tag{2-22}$$

where, A and B are the entropic and enthalpic contributions, respectively.

### 2.2.2. Phase Separation of Binary Polymer Blends

Among studies of polymer blends, the phase diagrams (T-$\phi$) of binary blends have been an interesting topic both in scientific and applied fields.[81]  Two types of phase diagrams for binary blends are most commonly observed as shown schematically in Figure 2.10.[77, 80]  Figure 2.10A represents a phase diagram with a lower miscibility gap or upper critical solution temperature (UCST) and Figure 2.10B is a schematic phase diagram with an upper miscibility gap or lower critical solution temperature (LCST). Both phase diagrams in Figure 2.10 exhibit a critical temperature ($T_C$), and binodal and spinodal regions.  At $T > T_C$ for UCST type phase diagrams, the two components are miscible at all $\phi$ and form a homogeneous phase; phase separation of blends occurs at temperatures below $T_C$ and depends on $\phi$.  For LCST type phase diagrams, two components are miscible at $T < T_C$ for all $\phi$, and demixing occurs at temperatures above $T_C$ and depends on $\phi$.  At any temperature, (see Figure 2.10) a binary mixture with

composition in the spinodal region is thermodynamically unstable and any small fluctuation in composition causes a decrease in free energy, leading to spontaneous phase separation. Meanwhile, blends with compositions between the spinodal line and the binodal line are metastable. Binary blends in the metastable regime can withstand small compositional changes but become unstable and phase separate when a sufficiently large composition/thermal fluctuation is applied. In this regime, phase separation proceeds by a nucleation and growth mechanism.
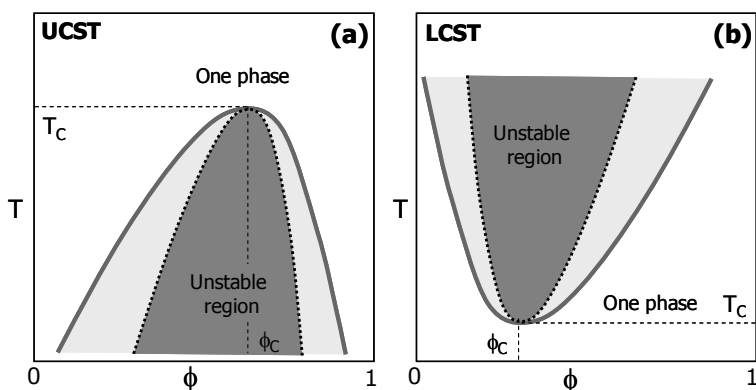


**Figure 2.10.** Schematic depictions of phase diagrams for asymmetric blends: (A) UCST and (B) LCST.[77, 80]
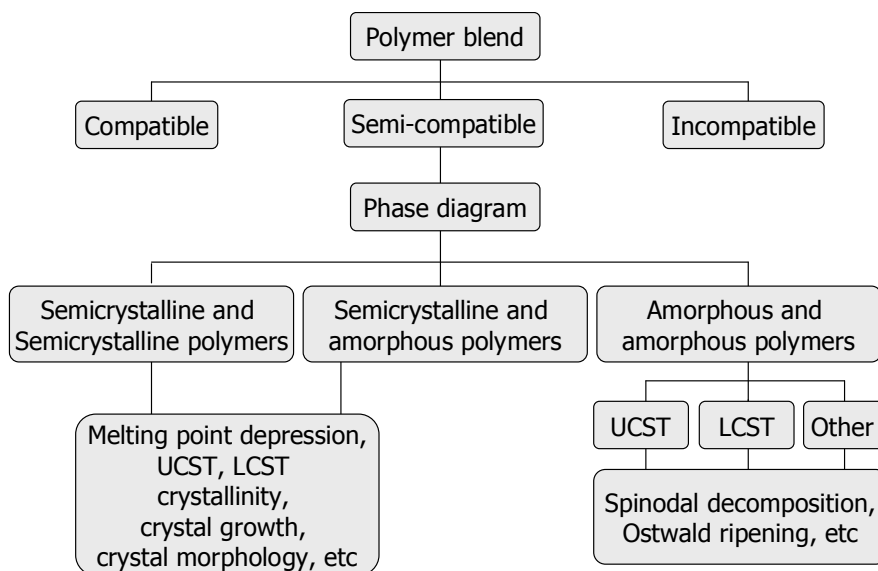
**Figure 2.11.** Classification of phase separated polymer blends.[82]


Phase separated polymer blends include amorphous-amorphous, amorphous-semicrystalline, and semicrystalline-semicrystalline blends as classified in Figure 2.11.[82, 83] For amorphous-amorphous polymer blends, phase separation can be induced by thermal or compositional changes, depending on the phase diagram for a specific system. Phase separation can take place either by spinodal decomposition or nucleation and growth mechanisms depending on the composition of the polymer blend.[84] The nucleation and growth (NG) type of phase separation occurs in the metastable region between the binodal and spinodal lines.[77, 80, 84] Blends with compositions in the metastable region are locally stable. Therefore, phase separation can only occur after a thermodynamic barrier for nucleation is overcome by a relatively large thermal and/or compositional fluctuation. The spinodal decomposition (SD) type of phase separation occurs spontaneously within the spinodal region because the blends in this region are unstable. [77, 80, 84]
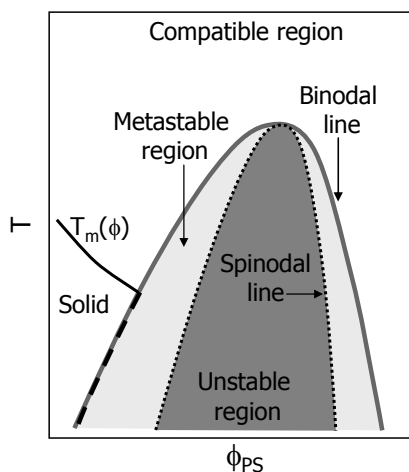
**Figure 2.12.** Schematic phase diagram of PCL-PS blends. $\phi$ is the volume fraction of PS.[85-89]

PCL blends with amorphous polymers belong to the category of amorphous-semicrystalline mixtures.   One pertinent example is the blend of PCL/polystyrene oligomer.[85-89]   In this blend system, the phase separation process is coupled with nonequilibrium growth of PCL crystals.  New types of spherulitic morphologies with a PS-rich layer at the growing interface are observed because of the competition between two nonequilibrium processes: phase-separation and crystallization.[85-89]   Furthermore, crystallization in blends can also be considered as a "phase separation" process because the amorphous components are strongly rejected from lamellar crystals and accumulated in the interlamellar regions.   The schematic depiction of a phase diagram for a PCL/PS oligomer is shown in Figure 2.12, where $T_m$ ($\phi$) represents a melting curve.  The melting point of crystalline components is governed by the fraction of amorphous liquid PS and decreases with increasing $\phi_{PS}$.  As indicated by Nishi at el., the binodal line below the melting curve can not be strictly defined in an equilibrium phase diagram.[85-87]

**2.3. Diffusion of Polymer Chains**

To guide the studies of PCL crystallization in PCL-based blends as Langmuir films, another concept, polymer diffusion, needs to be reviewed. Diffusion is a transport process, driven by a thermodynamic force which arises from chemical potential gradients.[77] The diffusion process in a polymer solution can be described by the self-diffusion and mutual diffusion coefficients. Dynamic light scattering (DLS) can be used to measure the mutual diffusion coefficient. Meanwhile, self-diffusion coefficients can be determined by techniques such as forced Rayleigh scattering (FRS), fluorescence recovery after photobleaching (FRAP), neutron scattering, etc.[77] Diffusive properties of polymer chains in polymer materials are very complex; many experimental studies and theoretical investigations about polymer diffusion have been documented. The basic concepts are reviewed and summarized in this section.

**2.3.1. Self-diffusion Coefficient**

Self-diffusion arises from the zigzag migration of the center of mass of a polymer molecule, which is caused by the corporative movement of segments and driven by entropy.[77] The self-diffusion coefficient is defined by Eq. 2-23:

$$D_s = \lim_{t \to \infty} \frac{< [r_1(t) - r_0(0)]^2 >}{6t} \tag{2-23}$$

which tracks the center of mass of the polymer chain as a function of time, t. In quiescent solution, the self-diffusion coefficient is also associated with the friction coefficient, $\zeta$, through the Nernst-Einstein equation:

$$D_s = \frac{k_B T}{\zeta} \tag{2-24}$$

where $\zeta$ is defined by $F = \zeta v$, indicating that a constant force, F, is required to drag a suspended polymer molecule through a viscous medium at a constant velocity, v.

Because other molecules tend to interrupt the free diffusion of a given polymer molecule, it is obvious that the self-diffusion coefficient depends on solution concentration. The concentration dependence of the friction coefficient is given by

$$\zeta = \zeta_0 (1 + \zeta_1 c + ....) \tag{2-25}$$

where $\zeta_0$ is the friction coefficient in the dilute solution limit and $\zeta_0\zeta_1$ (>0) is the first-order concentration coefficient. Substituting Eq. 2-25 into Eq. 2-24 yields

$$D_s = \frac{k_B T}{\zeta} = \frac{k_B T}{\zeta_0 (1 + \zeta_1 c + ....)} \tag{2-26}$$

Thus, at very low concentration, a series expansion can be used on the denominator of Eq. 2-26 to show that $D_s$ decreases linearly with concentration:

$$D_s \sim \frac{k_B T}{\zeta_0} (1 - \zeta_1 c) \tag{2-27}$$

In addition, Stokes showed that $\zeta$ for a polymer with a Stokes' radius $R_s$ in a solvent of viscosity, $\eta_s$ is given by $\zeta = 6\pi\eta_s R_s$. Thus, Eq. 2-26 at infinite dilution yields the Stokes-Einstein equation:

$$D_s = \frac{k_B T}{6\pi\eta_s R_s} \tag{2-28}$$

The diffusion process becomes more complex in multi-component systems such as binary or ternary solutions consisting of a solvent and more than one polymer species. In these systems, one of the polymeric components can be selected as a tracer. The concentration of the tracer component is very low in solutions of other polymers (matrix

components).  The self-diffusion coefficient of the tracer component is called the tracer

diffusion coefficient, $D_{tr}$.[77]  $D_{tr}$ is a function of the matrix polymer concentration, chain

length of the matrix polymer, chain length of the tracer molecule, and temperature.  $D_{tr}$

can also be measured by dynamic light scattering.

## 2.3.2. Mutual Diffusion Coefficient

Another concept defined for understanding diffusive process is mutual diffusion

coefficient, $D_m$, or known as the interdiffusion coefficient.  $D_m$ is a characteristic

parameter for the system and not for either polymer component or solvent.  The mutual

diffusion coefficient for two spherical particles, 1 and 2, is defined as

$$D_m = \lim_{t \to \infty} \frac{< [r_1(t) - r_2(0)]^2 >}{6t}$$

(2-29)

where $< [r_1(t) - r_2(0)]^2 >$ is the root mean square displacement of particle 1 at time t

relative to the position of particle 2 at t = 0.  One should note that $D_m$ is not directly

associated with the motion of polymer molecules relative to the solvent.  Mutual

diffusion is a very complex process, which depends on the solution concentration,

temperature, molar mass, and thermodynamic interactions of solute-solute or solute-

solvent.[77]  Dynamic light scattering is used to measure $D_m$ because the instrument does

not distinguish one solute from another.  In the dilute solution regime, c $\ll$ c$^*$, the

concentration dependence of $D_m$ is given by Eqs. 2-30 and 2-31:

$$D_m = D_0 (1 + k_D c + ....)$$

(2-30)

$$k_D = 2 A_2 M - \zeta_1 - v_{sp}$$

(2-31)

where $D_0$ is the diffusion coefficient of isolated solute in the dilute solution limit, $A_2$ is

the second virial coefficient, $\zeta_1$ is the friction coefficient as defined in Eq. 2-25, M is

molar mass, and $v_{sp}$ is the specific volume of the polymer in solution, indicating the increment in the solution volume when a unit mass of the polymer is added. In good solvent conditions, $2A_2M > \zeta_1 + v_{sp}$; $D_m$ increases with increasing concentration. The second virial coefficient, $A_2$, decreases in poor solvent conditions and eventually $k_D$ becomes negative. $D_m$ measured in the semidilute regime of $c \gg c^*$ are called cooperative diffusion coefficients, $D_{coop}$, indicating the cooperative movement of segments within a blob. In semidilute polymer solution, the blob is defined as a spherical regime between two neighboring entanglement points on the same chain. $D_{coop}$ is associated with blob size, $\xi$, as given by Eq. 2-32:

$$D_{coop} = \frac{k_B T}{6\pi\eta_s\xi} \tag{2-32}$$

where, $\eta_s$ is the viscosity of solvent. Correlation length, $\xi$, decreases with increasing solution concentration, so $D_{coop}$ becomes faster. $D_{coop}$ increases as $D_{coop} \sim \xi^{-1} \sim c^{\upsilon/(3\upsilon-1)}$ because $\xi \sim c^{-\upsilon/(3\upsilon-1)}$. In a good solvent, $D_{coop} \sim c^{3/4}$, while in theta solvents, $D_{coop} \sim c$. A key feature of the semi-dilute solution is that $D_{coop}$ is independent of molar mass.[77]

Diffusion can also be defined as a kinetic process. Figure 2.13A shows a container having solutions with different concentrations separated by a partition. The solutes start to move from the high concentration side (right) to the low concentration side (left) once the partition is removed. The boundary line of concentration becomes fuzzy (Figure 2.13B) and eventually the concentration becomes uniform in the entire container as seen in Figure 2.13C. The driving force of this process is the spatial concentration variation, $c(r)$. The rate of transfer is called a flux, $j(r)$, which is defined as the mass of the solute that moves across a unit area in a unit time as given by Eq. 2-33:

$$j(r) = c(r)v(r) \qquad (2\text{-}33)$$

where v(r) is the velocity of solution motion in the same direction as the flux. The locally small concentration variation can be represented by concentration gradient, $\nabla c(r)$. The flux is proportional to $\nabla c$ in Fick's law:

$$j = -D\nabla c \qquad (2\text{-}34)$$

Diffusive processes following Fick's law are called Fickian diffusion processes with a diffusion coefficient, D.
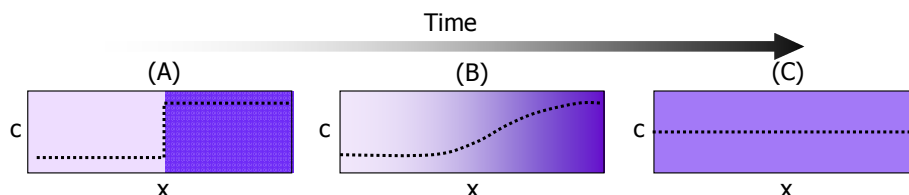


**Figure 2.13.** Concentration profiles (a) before partition removal, (b) during equilibration, and (c) at equilibrium.[77]

### 2.3.3. Molar Mass Dependence of Diffusion

The molar mass dependence of polymer diffusion in melts has been well documented.[90-93] The most important models for diffusion in non-swollen systems are summarized here.

### 2.3.3.1. Rouse Model and Zimm Model

The Rouse model[94] employs a bead-spring treatment of the polymer chain. It assumes that the beads have no excluded volume and no hydrodynamic interactions exist between the beads. The polymer chains in this model are isolated free-draining chains under theta conditions. The center of mass of the spring-bead chain exhibits diffusive motion for all

time scales. The center of mass diffusion coefficient obtained from the Rouse model is given by Eq. 2-35 to describe the self diffusion of polymer chains with N connected beads:

$$D_{Rouse} = \frac{k_B T}{N\zeta} \sim N^{-1} \tag{2-35}$$

where each bead moves independently of the other beads with a friction coefficient, $\zeta$. However, the Rouse model cannot account for perturbations of chain conformations by entanglements, even though the hydrodynamic interactions are almost screened out at very high concentrations and in melts.[77, 94] Upon decreasing the concentration below the entanglement point, the molar mass dependence of $D_s$ is proportional to $N^{-1}$ as proposed by the Rouse model. Once the concentration decreases to very dilute regimes, hydrodynamic interactions must be considered. The molar mass dependence of $D_s$ starts approaching $N^{-\nu}$ ($0.5 < \nu < 0.6$) as proposed by Zimm for isolated non-draining chains.

Zimm modified the Rouse model by considering hydrodynamic interactions between beads.[95] The center of mass diffusion coefficient obtained from the Zimm model is given by Eq. 2-36 and 2-37 for theta and good solvent conditions, respectively.

$$\text{In theta solvent (ideal chains): } D_{Zimm} = \frac{8}{3(6\pi^3)^{1/2}} \frac{k_B T}{\eta_s b N^{1/2}} \sim N^{-1/2} \tag{2-36}$$

$$\text{In good solvent (real chains, } \nu = 0.59 \text{ or } 0.6\text{): } D_{Zimm} = \frac{k_B T}{\eta_s b N^{\nu}} \sim N^{-\upsilon} \tag{2-37}$$
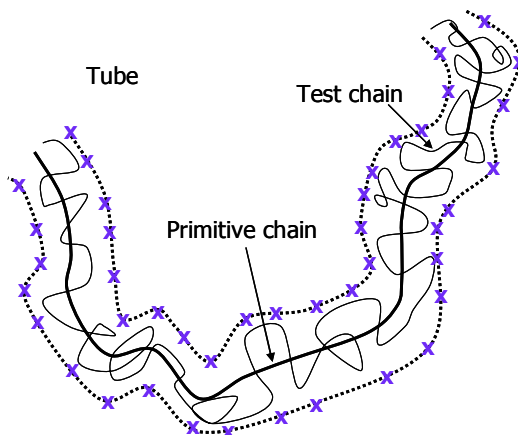
**Figure 2.14.** The test chain trapped in a tube.[77]


### 2.3.3.2. Tube Model and Reptation Theory

Polymer melts with molar masses above the critical molar mass for entanglements, and semidilute and concentrated polymer solutions are highly viscous and entangled. Tube models and reptation theory were proposed by de Gennes[96] and applied to semidilute solutions and polymer melts by Doi and Edwards in the late 1970s.[97-99] In the tube model, a single chain, labeled as the test chain, is selected from solution as shown in Figure 2.14. It is assumed that the test chain is trapped in a tube, which is created by the surrounding chains. These neighboring chains prevent the test chain from exiting the constrained tubelike region. The crosses in Figure 2.14 indicate the intersections of surrounding chains with the surface of tube. The tube model assumes that: 1) the test chain is only allowed to move along the tube region and never moves out of the tube region; 2) the zigzag movement of the test chain in the tube is similar with segments wiggling with a blob; and 3) the head of a test chain can decide the next direction freely. Once the head portion moves forward a bit, a new section of tube is added immediately and the rest of the tube follows the head on its existing path. This type of motion is

termed reptation. However, the change of tube length with time is always small. The centerline of the tube region is defined as a primitive chain as seen in Figure 2.14. At each step time, the head of the primitive chain moves a distance $b_t$ to explore a new direction. The movement of the rest of the chains follows its existing path in the tube. According to the tube model and reptation theory,[96-99] the center of mass diffusion coefficient is given as

$$D_T = \frac{k_B T b_t^2}{N^2 \zeta b^2} \sim N^{-2} \tag{2-38}$$

The center of mass diffusion coefficient discussed above is used to describe the self-diffusion of polymer chains in entangled solutions.

## 2.4. Crystallization of Semicrystalline Polymers

Understanding the nucleation and growth process is one of the key points for understanding PCL crystallization at the A/W interface. Although previous well-developed theories of polymer crystallization may not be directly applicable to understanding crystallization in Langmuir monolayers, some features of bulk crystallization may provide useful analogies and insight into crystallization at the A/W interface. Thus, this section addresses some fundamental concepts of semicrystalline polymer crystallization.

### 2.4.1. Introduction

The crystalline state is defined as a state exhibiting a melting temperature, $T_m$ (a first-order phase transition), and an X-ray scattering pattern with sharp reflections. At the melting temperature, heat has to be added until all well-ordered crystallites have been transformed into a disordered melt state. $T_m$ is usually controlled by factors such as

polarity, hydrogen bonding, molar mass, etc. $T_m$ can be conveniently observed through thermal analysis. Differential scanning calorimetry (DSC) has been a popular method for quantitative thermal analyses since it can easily provide $T_m$, as well as the heat of fusion, $\Delta H_f$, which is given by the total area under the $T_m$ peak. The glass transition temperature, $T_g$, is a characteristic of the amorphous state, which is still present in semicrystalline polymers. However, it is usually difficult to observe $T_g$ in highly crystalline polymers since only a very small amount of amorphous substance is present, leading to a weak thermal signal.[100]

The development of crystallinity normally requires that the polymer chains can be extended in a low energy conformation (a helix, or a zigzag) and be generally packed with chain axes parallel to each other. From the view point of structural regularity, isotactic and syndiotactic polymers are usually easier to crystallize, whereas atactic polymers usually do not crystallize. Crystallizable polymers usually have very small crystalline regions, which are interconnected by an amorphous phase such that the crystallinity of polymers ranges between 0% and 95%. Polymer chain arrangements also exhibit some defects such as occasional and irregular kinks or folds outside crystalline regions. Thus, polymer materials are classified as non-crystalline and semicrystalline materials.[100, 101]

For melts, polymer crystallization initially starts from a nucleation site. Nucleation is usually defined as the formation of the smallest crystalline entity due to density fluctuations in supercooled melts.[102] The further growth of these crystallites is thermodynamically favored. Nucleation may be classified as primary, secondary or tertiary nucleation.[103] Primary nucleation refers to the initial process of nuclei formation.

The thermodynamic description of the crystallization process starts with Eqs. 2-39 and 2-40:

$$\Delta G = G_{crystal} - G_{melt} \qquad (2\text{-}39)$$

$$\Delta G = \Delta H - T\Delta S \qquad (2\text{-}40)$$

where $\Delta G$ is the total Gibbs free energy of crystallization, and $\Delta H$ and $\Delta S$ are the total enthalpy and entropy of crystallization, respectively. $G_{crystal}$ is the overall free energy of the crystal and $G_{melt}$ is the free energy of the same amount of material in the melt state. Small crystallites must have a large specific surface area, $A$ with specific surface free energy, $\gamma^*$. Hence, the overall free energy of a crystal can be written as

$$G_{crystal} = G_{bulk} + \sum A\gamma^* \qquad (2\text{-}41)$$

where $G_{bulk}$ is the free energy of the crystal disregarding surface effects. If one ignores surface effects, the free energy difference between the bulk crystal and its melt is defined as

$$\Delta G_c = G_{bulk} - G_{melt} \qquad (2\text{-}42)$$

Thus the total free energy change of crystallization can also be written as

$$\Delta G = \Delta G_c + \sum A\gamma^* \qquad (2\text{-}43)$$

Furthermore, if one assumes a spherical geometry for a crystal of radius, R, the total free energy change of crystallization becomes

$$\Delta G = \frac{4}{3}\pi R^3 \Delta G_c^V + 4\pi R^2 \gamma^* \qquad (2\text{-}44)$$

At T < T$_m$, $\Delta G_c^V$ is negative and the specific surface free energy, $\gamma^*$, is positive for all temperatures. In Eq. 2-44, there is a competition between heat released by the growing crystals (favorable) and higher surface energy (unfavorable). Initially (small R), the

surface energy term dominates the process and nucleation is thermodynamically unfavorable. However, there is a finite probability that some nuclei will grow larger than the critical radius, R*, corresponding to the maximum $\Delta G$ in Figure 2.15. Nuclei with sizes less than R* are called subcritical nuclei or embryos. Nuclei that are larger than R* but still possess positive $\Delta G$ are called supercritical nuclei. Nuclei with a negative $\Delta G$ value are called stable nuclei or small crystals.[73] Thus, a thermodynamically stable crystal of sufficient size must be grown through a path from positive to negative $\Delta G$ as illustrated in Figure 2.15. The free energy barrier to crystallization can be overcome by local random density fluctuations, or local order in the melt. The larger the required size of stable nuclei, the longer the required time for the nucleation process.
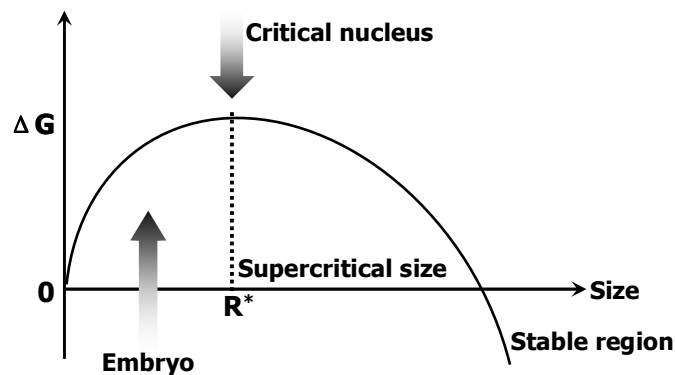


**Figure 2.15.** Schematic illustration of the nucleation process: the change in free energy $\Delta G$ as a function of size.

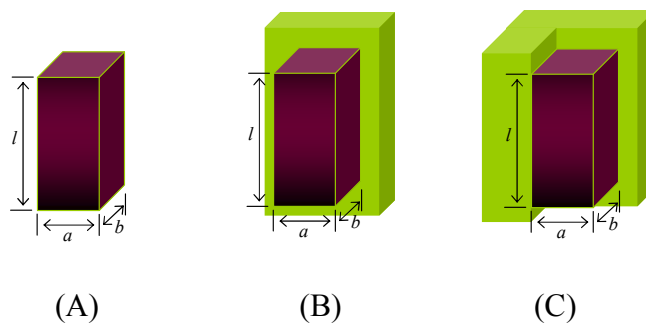(A)                    (B)                    (C)

**Figure 2.16.** Types of nuclei: (A) Primary nucleus, (B) secondary nucleus, and (C) tertiary nucleus.

Primary nucleation can be homogeneous or heterogeneous. The formation of initial nuclei in the absence of a second phase is termed homogenous nucleation. The nucleation initiated by any foreign particle or a second surface from the same polymer is referred to as heterogeneous nucleation. A foreign surface usually reduces the activation energy barrier for the formation of a stable nucleus since the creation of the interface between the polymer crystal and the foreign surface is easier than the creation of a free polymer crystal surface.[103] If heterogeneous nucleation is initiated by entities having the same composition as the crystallizing polymer, it is called self-nucleation, such as nucleation induced by pre-existing nuclei.

Secondary nucleation refers to a process whereby a new layer of crystal deposits on a molecularly smooth crystal surface. Secondary nucleation has a lower free energy barrier than primary nucleation since the newly created specific surface area is smaller. Tertiary nucleation is defined as fresh crystal growth at an edge as seen in Figure 2.16. Tertiary nucleation exhibits the smallest free energy barrier due to the smallest specific surface

area, so the relative difficulty for different nucleation processes yields the order: primary nucleation > secondary nucleation > tertiary nucleation.

The shape, the chain-orientation, and the size of the crystals not only depend on the structural characteristics of the polymers, but also on processing conditions.[102] Crystallization can be induced by evaporating a dilute solution, cooling a molten polymer, annealing processes, or drawing processes.  Annealing is a process in which the crystallinity is formed by heating the substance at a specified temperature in vacuum or an inert atmosphere to prevent oxidation.  Stretching a polymeric substance at a temperature above $T_g$ may also induce crystallization in a process called drawing.[101]

## 2.4.2. The Fringed Micelle Model

The earliest evidence of semicrystalline structures in polymers was discovered in X-ray and electron diffraction patterns, where two overlapping yet distinct diffraction patterns indicted that both amorphous and crystalline regions coexisted in the polymer.[101] Hermann and Gerngross postulated the first model, the "fringed micelle model," to describe the crystalline structure of natural rubber (Figure 2.17).[104]  According to this model, the fringed micelles were present in a "sea" of amorphous phase and the length of the crystallites was on the order of 100 Å.  The "fringes" are the regions of the chains crossing from the crystalline region to the surrounding amorphous phase.  Each polymer chain thus passes in and out of the crystalline and amorphous phases several times since the chain length is longer than the crystallites in at least one dimension.  This model has been successfully used to describe the coexistence of amorphous and crystalline phases and the behavior of drawn fibers; however, it has failed to explain the formation of actual crystalline structures such as spherulites, for most semicrystalline polymers.[101]
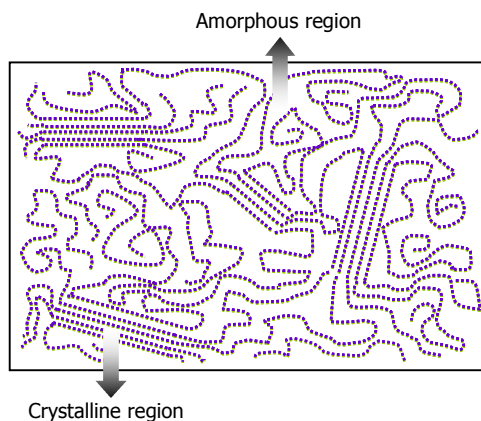
**Figure 2.17.** Schematic diagram of the fringed micelle model for semicrystalline polymers.

### 2.4.3. Crystallization from Dilute Solution

Crystallization from dilute solution can produce rather regular crystals, usually called single crystals. Single crystals have a large extension in two dimensions and a uniform thickness. One classical sample is the PE single crystal prepared by Keller from extremely dilute xylene solutions.[105] From Keller's study onward; polyethylene has become a popular model system for studying single crystals. High density polyethylene ($M_w$ = 10 kg·mol$^{-1}$, $M_w/M_n$ = 1.02) single crystals have also been obtained by isothermal crystallization in a tetrachloroethylene solution.[106] The thickness of the PE single crystal is on the order of 100 to 200 Å, which was significantly smaller than the 2000 Å contour length of the polymer chain. Thus, the polymer chains must back-fold and re-enter into the crystals multiple times. Previous investigations showed that the unit cell structure of PE contains two mers.[107] The unit cell is orthorhombic with dimensions of a = 7.40 Å, b = 4.93 Å and c = 2.53 Å. Two models of chain reentry into crystals were immediately proposed to explain the growth of single crystals. One is the folded-chain model

illustrated in Figure 2.18A.[108]  According to this model, the polymer chains tightly and regularly fold back and forth and the single crystal growth occurs through the lateral deposition of regularly folded-chains in the plane.  According to the switchboard model, which was later proven to be wrong, the energy of tight folding is so high that adjacent reentry is forbidden, and polymer chains fold and enter the crystal randomly as depicted in Figure 2.18B.[109] Both of the above models represent two limiting cases, the actual system could be more complex and likely lies somewhere between the two limiting cases. In addition, the polymer crystals are not always perfect.  Examples of some defects in crystallites (loose loops, tie chains, etc.) are illustrated in Figure 2.19.[83]
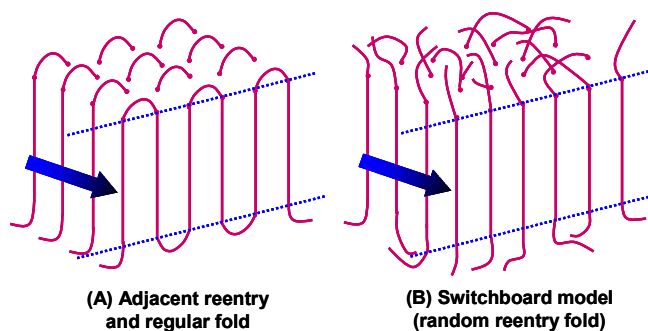


**(A) Adjacent reentry
and regular fold**

**(B) Switchboard model
(random reentry fold)**

**Figure 2.18.** Schematic illustration of the folded-chain and switchboard model. (A) Folded-chain model: tight, adjacent reentry into a polymer crystal, and (B) Switchboard model: random reentry into the crystal.
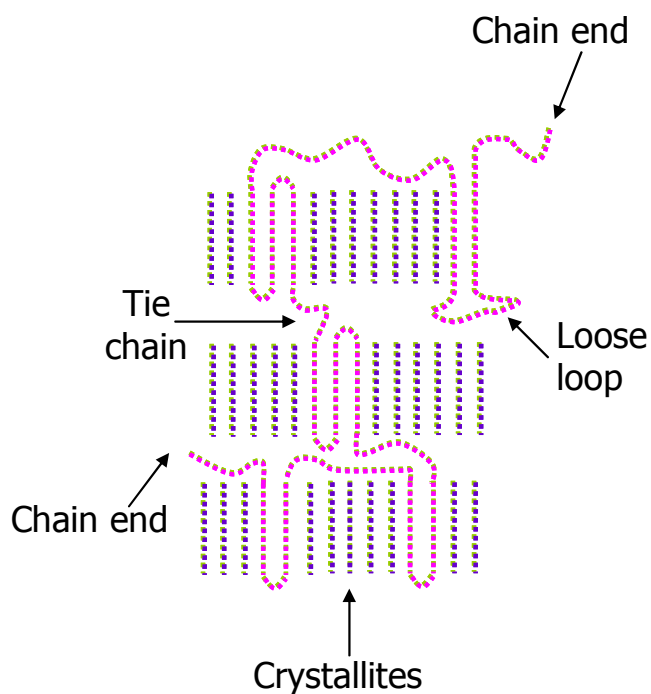
Chain end

Tie chain

Loose loop

Chain end

Crystallites

**Figure 2.19.** Schematic illustration of a polymer chain in folded-chain lamellar crystals.

Various single crystal structures of 17 polymers have been reviewed by Livingston.[110] Single crystal morphologies of biodegradable aliphatic polyesters have also been reported by Iwata *et al.*[111] PCL multilamellar crystals were prepared from dilute solutions of *n*-hexanol. The lamellar thickness of PCL single crystals is about 10 nm. The parameters of the crystal structure are consistent with that of the orthorhombic unit cell: $a = 7.48 \pm 0.02$ Å, $b = 4.98 \pm 0.02$ Å and $c = 17.26 \pm 0.03$ Å, which were obtained from previous X-ray diffraction studies.[112-114]

Two conformations for PCL in crystal structures as depicted in Figure 2.20 have been suggested by previous studies: a nonplanar conformation (Figure 2.20A);[112] and a planar conformation (Figure 2.20B).[113]   In the nonplanar model the carbonyl groups of two neighboring chains in the unit cell are not located at the same level to lower the internal energy of the stem region.  Hu *et al.* showed that the nonplanar conformation is more reasonable than the planar model according to their improved crystallization technique and electron diffraction data.[114] Measured unit cell parameters from electron diffraction patterns are in agreement with previous X-ray studies. The crystal structure of PCL is similar to polyethylene, but the chain is twisted slightly from a fully extended conformation.
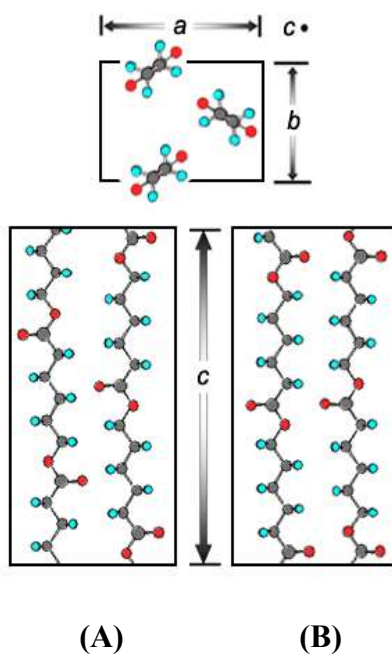


**(A)**                    **(B)**

**Figure 2.20.** Two models for PCL crystal structures: (A) the nonplanar conformation, and (B) the planar conformation.[112-114]

It could be easier to produce regular lamellar crystals from dilute solution than from melts since the polymer chains are fully separated from each other.  Like crystals grown from dilute solution, similar lamellar crystallites are also present in spherulitic crystals grown from the melt state.  Both the thickness and shape of lamellae can vary with the degree of undercooling, $\Delta T = T_m^0 - T_x$, where $T_m^0$ is the equilibrium melting temperature of an infinitely large crystal and $T_x$ is the isothermal crystallization temperature.  Greater undercooling produces thinner crystals; meanwhile the thicknesses of lamellar crystals affect the observed melting temperature.  $T_m^0$ is the melting point of an infinitely large crystal in equilibrium with the normal polymer liquid, it is always greater than the actual melting point.  Hence it is impossible to directly measure $T_m^0$.

## 2.4.4. Spherulitic Crystal Growth from Melts

Crystallization out of the melt state is different from crystallization out of dilute solutions because of the effects of chain entanglements in the melt.  Consequently, the possibility of regular chain folding across the entire growing surface is very low except for the case where the driving force and growth rate are small enough that a single polymer chain can cast off all of its neighbors and directly attach itself onto the growing surface.[115]
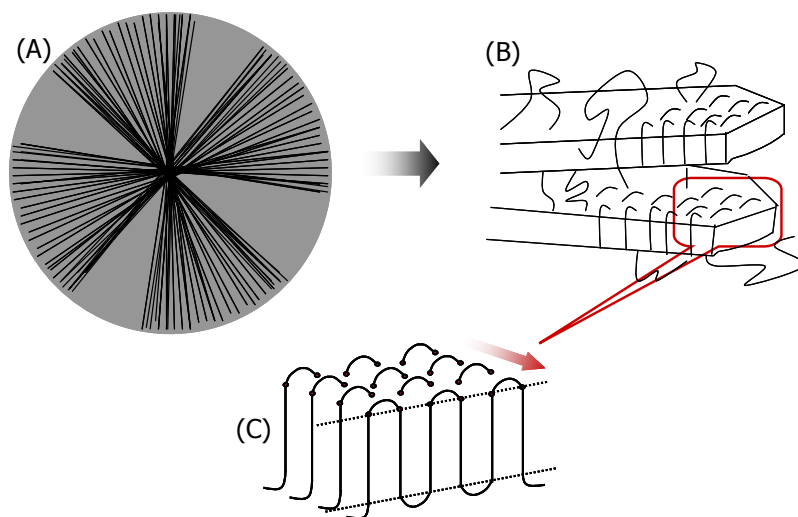
**Figure 2.21.** Schematic illustrations of a spherulite: (A) ideal illustration of a spherulite; (B) spherulitic growth fronts, and (C) chain folding lamellae.

When polymers crystallize from a melt, the most commonly observed morphologies are spherulites, which are aggregates of many small lamellae (see Figure 2.21B). Chain folding in crystallites is also shown in Figure 2.21C. Figure 2.21A shows the ideal schematic illustration of spherulites during crystallization from a melt. The long axes of the individual lamella are oriented along the radius of the growing spherulite and the axes of the folding chains in each lamella are roughly perpendicular to the spherulite's radius. In spherulites, one polymer chain can be present in more than one lamella and lamellar structures are separated by amorphous phase as seen in Figure 2.21B.[103] Spherulitic morphologies are usually observed for PCL crystallized isothermally in melts.[2, 116]

Spherulitic growth rates can be estimated by measuring a spherulite's radius as a function of time by optical microscopy. From a kinetic point of view, the spherulitic growth rate is dependent upon where $T_x$ is located in the thermal window (between $T_m^0$ and $T_g$).[117] When spherulite growth rates are plotted as a function of $T_x$, a maximum

linear growth rate is often obtained in the middle of the thermal window as shown in Figure 2.22. At small degrees of undercooling ($\Delta T = T_m^0 - T_x$, the right-hand side of Figure 2.22), crystal growth is nucleation controlled and linear growth rates increase with increasing $\Delta T$ up to the maximum growth rate, $G_{max,}$. After $G_{max,}$ further decreases in $T_x$ approach $T_g$, and limited chain mobility causes a decrease in the growth rate as $\Delta T$ increases. In this region, the growth rate is controlled by diffusion as seen in Figure 2.22 (light gray or left-hand side).
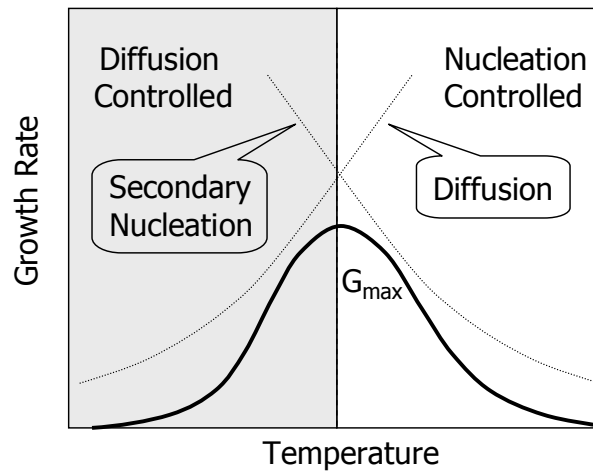


**Figure 2.22.** Dependence of the spherulitic growth rate on crystallization.

### 2.4.5. Polymer Crystallization in Thin Films

It is well-known that the confinement of semicrystalline polymers in thin films can significantly alter properties such as molecular mobility,[4, 5] the glass transition temperature,[6, 7] chain orientation,[8-10] etc. For instance, the interfacial interactions between films and substrates may alter the transport of polymer molecules to the growth

fronts of crystallizing lamellae, thereby altering growth rates, morphologies and melting temperatures for crystals grown in thin films.[8-23, 118]

Previous studies of PCL crystallization in PCL/polyvinyl chloride spincoated films[10] reveal that isothermal crystallization rates decrease when the film thickness is less than 1 μm. A decrease in the isothermal crystallization rate was also observed for pure PCL crystallized in spincoated films with thicknesses less than 30 nm. For example, the growth rate is about one-half the bulk growth rate at crystallization temperatures of 50 °C and 54 °C for 15 nm thick films; while for 6 nm thick films, the growth rate decreases dramatically, resulting in a growth rate that is similar at both temperatures.[9] In contrast, growth rates observed for PCL films with thicknesses in the range of 30-200 nm at both 50 °C and 54 °C are consistent with measurements for thicker films up to 2000 nm and bulk crystallization. Comparable results have also been reported for poly (di-n-hexysilane), isotactic-polystyrene and poly(ethylene oxide).[7, 22, 118-122] In addition, nonlinear growth of PCL crystals is ultimately observed for 15 nm and 6 nm thick PCL films after a sufficient period of growth.[9] All of these previous studies indicate that the diffusion of polymer chains from the surrounding melt to the growth front becomes a determining factor for crystal growth in two-dimensional (2D) constrained geometries as the film thickness decreases below a certain threshold thickness value.[7-23, 118-122] As a consequence, typical diffusion-limited morphologies, including dense-branched morphologies, dendrites, and fractals, are observed in sufficiently thin films for different polymers. [7-23, 118-122]
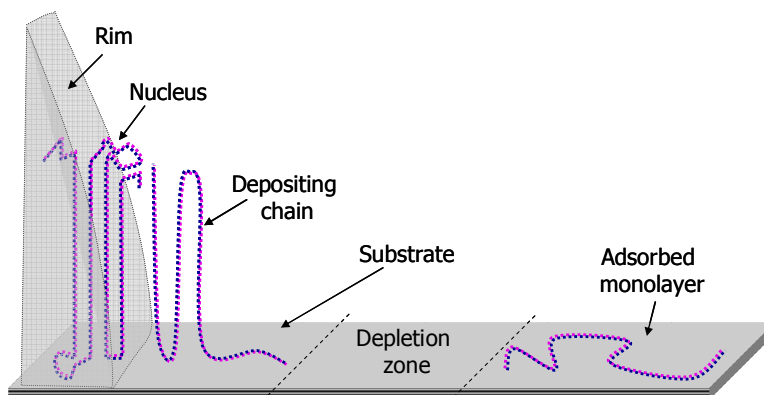
**Figure 2.23.** Diffusion of polymer chains from an adsorbed monolayer to a crystal surface.

Dendritic fingers of poly(ethylene oxide) (PEO) crystals are observed in metastable monolayers as PEO film thickness approaches ~ 10 nm, while single crystal and spherulitic crystal morphologies are observed in thicker films.[12-16] As noted by Reiter *et al.*, dendritic growth of PEO occurs in the metastable monolayer left behind in holes during dewetting.[12-15] The polymer chains initially attach onto the nuclei formed at the rims of the dewetting holes as shown in Figure 2.23. The growth of flat-on lamellae is energetically favored because the vertically stretched configuration increases the energy released during crystallization. The change of conformation from flat adsorbed chains to vertically folded chains leads to a depletion zone surrounding the crystal growth front. The molecules moving across the depletion zone from the monolayer region preferentially attach to the closest site on the crystal surface. Thus, this site becomes even closer to the molecular reservoir in the monolayer region and grows faster, leading to the formation of a dendritic finger. A detailed discussion of sidebranching and the dendritic growth mechanism will be provided later in this chapter.

More recently, adding amorphous poly(methylmethacrylate) (PMMA) into PEO has been used to "tune" the crystal morphologies of PEO in mixed thin films.[17-20, 118] The morphological transition from spherulites, to needles, and dendrites is observed when the composition varies from 90 to 30 wt% PEO.[118] In addition, adding a fixed amount of clay (5% by weight relative to the total polymer mass) to the PEO/PMMA blends yields seaweed dendritic growth (50 wt% PEO), symmetric dendritic growth (30 wt% PEO), and fractal dendritic growth (20 wt% PEO).[18, 19] Moreover, previous studies also suggest that both crystallization temperature and blend composition may play similar roles on the morphological evolution of PEO crystals in PEO/PMMA blend films because both parameters affect diffusive properties (diffusion coefficient, diffusion length, etc.) of the crystalline component.[18, 19] Taguchi *et al.* extensively investigated the crystal growth of isotactic polystyrene (it-PS) in ~ 11 nm thick film.[122] Dendritic crystals with sixfold symmetry and compact seaweed morphologies are observed with decreasing crystallization temperature. Similar diffusion-limited morphologies have also been reported for other polymer systems such as poly(styrene-ethyleneoxide),[12] poly(trifluoroethylene),[123] poly(ethylene terephthalate),[124] and poly(S-lactide).[125]

From the above review of polymer crystallization, the following points should be highlighted:

1. Polymer chains order themselves in a thermodynamically favorable conformation in the crystalline region.

2. Both crystalline and amorphous regions coexist in semi-crystalline polymers obtained from the melt or concentrated solutions. Crystal growth from the melt or concentrated solutions is usually spherulitic under quiescent conditions.

3. Crystallization from dilute solution usually produces more regular crystals than crystallization from melts. For sufficiently dilute solutions, the polymer chains are fully separated from each other so that the effects of chain entanglements on crystallization can be reduced, unlike the cases of crystallization from melts or concentrated solutions.

4. For polymer crystallization in thin film geometries below a threshold thickness, the diffusion of polymer chains to the crystal growth fonts becomes a determining factor for both growth rate and morphologies because of the limited availability of crystallizable material in the vicinity of the growth fronts.  As a consequence, various diffusion-limited morphologies are observed in polymeric systems.

## 2.5. Dendritic Growth

Dendritic growth has been observed in many different systems from laboratory bench-top to mother nature such as metal alloys, polymers, and snowflakes.  Dendritic growth is a solidification process controlled by thermal and/or mass diffusion.  The morphology of dendritic crystals usually shows preferential sidebranches, reflecting the symmetry of the crystal structure. Dendritic tips are parabolic with secondary sidebranches developed along both sides of the dendrite.  In the past several decades, the dendritic solidification for small molecules has been widely studied and common models have been developed for describing the growth process.[126-128]  For polymeric systems, dendritic growth mechanisms still represents an interesting area that attracts widespread attention from both chemists and physicists.

**2.5.1. Mullins-Sekerka Instability**

One of the characteristic features of dendritic growth is sidebranching, which is driven by interfacial instability developed during the process of solidification. The studies of interfacial instabilities in crystal growth were initiated by Mullins and Sekerka.[126] Many theoretical and experimental studies were reported based on Mullins and Sekerka's initial contributions to the area.[127] The interfacial instability is usually driven by a diffusion field caused by either a thermal or concentration gradient around the growth fronts of solid phases.

The simplest case is solidification in a pure liquid. In this case, the heat generated during crystallization needs to diffuse back into the liquid phase or to the interface so that the solid phase can grow further into the metastable (supersaturated or supercooled) liquid phase. The temperature gradient thus generated leads to a thermal diffusion field near the boundary line between the two phases. The diffusion equations in both the solid and liquid phases are given by Eqs. 2-45 and 2-46:

$$\text{Solid phase: } D_{T,s}\nabla^2 T = \frac{\partial T}{\partial t} \tag{2-45}$$

$$\text{Liquid phase: } D_{T,l}^{'}\nabla^2 T = \frac{\partial T}{\partial t} \tag{2-46}$$

where $D_{T,s}$ and $D_{T,l}^{'}$ are thermal diffusion coefficients of the solid and liquid phases, respectively.

Another simple case is the diffusion field of chemical potential generated by concentration gradients during solidification in liquid mixtures. In this case, further growth of the solid phase at the solid/liquid interface is controlled by the diffusion of chemical components from the liquid to the growth fronts. Meanwhile, another

component has to diffuse away from the interface to the bulk liquid or along the boundary lines.  The diffusion of molecules in a field with a concentration gradient always takes substantially longer than thermal diffusion.  Thus, molecular diffusion near the interface becomes a governing factor for controlling the advance of the solid phase into the liquid phase.  The solidification process is essentially isothermal.  The diffusion equation describing the concentration gradient is given by Eq. 2-47 in terms of the chemical potential:

$$D_C \nabla^2 \bar{\mu} = \frac{\partial \bar{\mu}}{\partial t} \tag{2-47}$$

where $D_C$ is the chemical diffusivity.

   Both the thermal and chemical diffusion equations, Eqs. 2-45 through 2-47, can be solved by applying two boundary conditions at the interface: 1) the conservation boundary conditions (mass and energy) and 2) the Gibbs-Thomson boundary conditions. Here, the conservation boundary condition for the thermal diffusion field arises from heat conservation at the growing site of the interface.  The density difference between the liquid and solid phases needs to be ignored for simplification.   Meanwhile, mass conservation at the boundary is considered with respect to the diffusion field with concentration gradients.  The Gibbs-Thomson boundary conditions arise from the local equilibrium conditions at the solid/liquid interfaces.   More detailed mathematical analyses of these two diffusion equations can be found in the literature.[126, 127]   The solutions of Eqs. 2-45 through 2-47 are given by

$$\delta = \exp\left(-\frac{2z}{l}\right) - 1, \; z \geq 0 \;\; \text{(Liquid)} \tag{2-48}$$

$$\delta = 0, \; z \leq 0 \;\; \text{(Solid)} \tag{2-49}$$

where δ represents a dimensionless diffusion field generated in either a thermal (T) or chemical potential (μ) model.   The interface is flat prior to the formation of any protrusion at the point of z = 0.  The diffusion length is defined as $l = 2D/v$, where D represents the corresponding diffusion coefficient (thermal or chemical) in the liquid phase and the apex of the protrusion moves into the metastable liquid phase along the z-axis with an interfacial velocity v.  Detailed discussion of the linear equation for the moving point z indicates that the stability of the interface is determined by the overall effect of two opposing factors: 1) a destabilizing term proportional to the interface velocity, v, and 2) a stabilizing term associated with surface tension.[127]
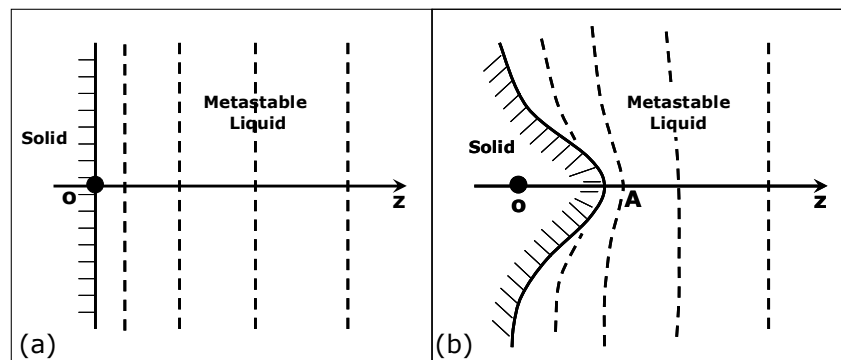


**Figure 2.24.**  Schematic depiction of the Mullins-Sekerka instability. The diffusion field is indicated by dashed lines.  Once a small protrusion forms at the interface as indicated by point A; it steepens the thermal gradient in the metastable liquid ahead of it.  The heat flows rapidly away from the surface of protrusion and the protrusion grows rapidly.

The schematic illustration of small protrusions generated in the corresponding diffusion fields is shown in Figure 2.24.  A small bump formed at the interface perturbs the diffusion field (dashed lines) near the apex as seen at in point A in Figure 2.24B.  As

a consequence, the heat generated during solidification can be removed faster near the apex (thermal diffusion), or the molecules from metastable liquid can easily move to the apex (chemical diffusion). Meanwhile, growth at the interface near but not at the apex of the protrusion is restricted and tends to melt because heat and solvent molecules accumulate in this region from the preferential growth at the apex. Therefore, the small protrusion grows faster and eventually gives rise to a dendritic finger. Once many sidebranches form along a surface, secondary sidebranches will grow along the principal sidebranches following the same sidebranching mechanism. The repetition of similar branching processes eventually leads to various dendritic morphologies under different solidification conditions. As indicated above, dendritic sidebranching is also controlled by the anisotropy of surface energy. The anisotropy of surface energy represents the orientation dependence of surface tension. Both experimental observations and theoretical studies in this aspect have been reported for small molecules.[128]

## 2.5.2. Diffusion-limited Growth of Polymer Crystals in Thin Films

Diffusion-limited growth for various polymeric systems has been reported in thin film geometries with thicknesses below certain threshold values.[9, 11-18, 118] Flat crystal surfaces may be destabilized by Mullins-Sekerka type instabilities in different diffusion fields leading to sidebranching. The diffusive properties of polymers together with the effects of anisotropy of surface energy eventually determine the crystal growth rate and morphologies.[129] In comparison with the small molecule systems, the dense-branched morphologies (DBM) are more commonly observed for polymer crystals than dendrites because of a relatively small anisotropy in surface energy. The dense-branched morphology is characterized by frequent sidebranching in the growth fronts without

specific orientation.  Dense-branched crystal morphologies can be composed of single crystals with weak orientational order[122] or disordered polycrystals as reported by Ben-Jacob and coworkers.[129 (b)]  It was found that the anisotropy of surface energy is only undercooling dependent and that the anisotropy decreases with increasing degrees of undercooling.  The anisotropy of the surface energy is a parameter that is difficult to quantify experimentally, but it is a commonly used parameter in theoretical calculations or simulations as reported by Kyu and coworkers.[130]  Both the experimental observations and simulation results for it-PS thin films indicate the morphological transition from hexagonal single crystals to dendritic crystals and a nonfaceted branched morphology is associated with a combination of the effects of the degree of undercooling and the anisotropy of the surface energy.[122, 130]  In PMMA/PEO blends, the anisotropy of the surface energy is not dependent on the composition of the crystalline component.[118]  The morphological transition from dendrites to DBM at a certain degree of undercooling is attributed to the effective noise level (the magnitude of the thermal and mass fluctuations), which was found to vary with the blend composition, undercooling, and molar mass of the PMMA component.[118]

Parameters such as molar mass, composition, temperature, etc. also affect the characteristic diffusion length as given by $l = 2D/v$, where D represents the self-diffusion coefficient of polymer chains. As $l$ is proportional to D and D usually decreases with decreasing temperature, a decrease in $l$ with temperature is expected.  Meanwhile, the growth rate increases with decreasing crystallization temperature as seen in it-PS thin film systems.[122]  Hence, the width of the sidebranches decreases with decreasing crystallization temperature.[122]

Furthermore, it is worth noting that the diffusion field near the interface between the liquid and the growing crystals is most commonly generated by either thermal or concentration gradients. However, as pointed by Taguchi *et al.*, the thermal diffusion may not give rise to interfacial instabilities in polymer systems because the growth rate is usually too slow to compete with thermal diffusion.[122] Thus, the effect of thermal diffusion can be ignored. Meanwhile, for dendritic crystallization of single component melts in thin films, a simple concentration gradient can be ruled out as well. Instead, Taguchi and coworkers pointed out that the diffusion field is generated by a gradient of melt thickness from the edge of growing crystals to the surrounding polymer melts, which destabilizes the interface and leads to dendritic branches. Nevertheless, the thickness gradient of polymer melts can be converted into an effective surface concentration of polymer chains. Thus, this type of diffusion field can still be treated as a "concentration gradient" and analyzed accordingly.

## 2.5.3. Dendritic Pattern Formation of Small Molecule Amphiphiles in Langmuir Monolayers

The nonequilibrium growth of condensed phases in Langmuir monolayers have been evaluated for small amphiphilic molecules such as N-dodecylgluconamide,[53] dioctadecylamine (DODA),[131] ethyl palmitate (EP),[131] ethyl stearate (ES),[131] diacetylene 10, 12-tricosadiynoic acid,[132] and D-myristol alanine.[133, 134] Nonequilibrium growth of liquid-condensed phases or crystalline solid phases starts from a small nuclei formed in a supersaturated monolayer during compression. The interfacial instabilities usually occur at the interface between the liquid-expanded and liquid-condensed phases or liquid-expanded and solid phases during monolayer compression. Various domain structures

have been observed including fractal, dense-branched, and dendritic morphologies.[131]  At

the A/W interface, the thermal diffusion model cannot apply because the heat released

during the phase transition can be instantaneously adsorbed by the aqueous subphase,

which acts as an isothermal reservoir. Recent experimental and theoretical studies

performed by Flores and coworkers indicate that the chemical potential is responsible for

the interfacial instabilities, while line tension tends to stabilize the surface.[131]  In addition,

the nonequilibrium morphology of liquid-condensed phases can also be determined by

the overall effects of dipole-dipole repulsive interactions and line tensions.[131]  Although

Flores and coworkers presented a reasonable explanation for the instabilities generated

along LE/LC phase boundaries, their mathematical analyses are over simplified by

ignoring the hydrodynamic coupling between the moving amphiphiles and the subphase.

In particular, the compression rate dependent mass diffusion in Langmuir monolayers

makes the dynamics of Langmuir monolayers more complex than classical molecular

systems.   The growth of polymer crystals in supersaturated Langmuir monolayers

becomes even more complicated than small molecules if one considers the controlling

parameters for polymer crystallization such as molar mass, blend composition,

crystallization temperature, etc. during compression experiments at the A/W interface.

Growth of PCL dendritic crystals at the A/W interface was first reported by our group

and many facets of PCL crystallization in Langmuir films will be presented in this
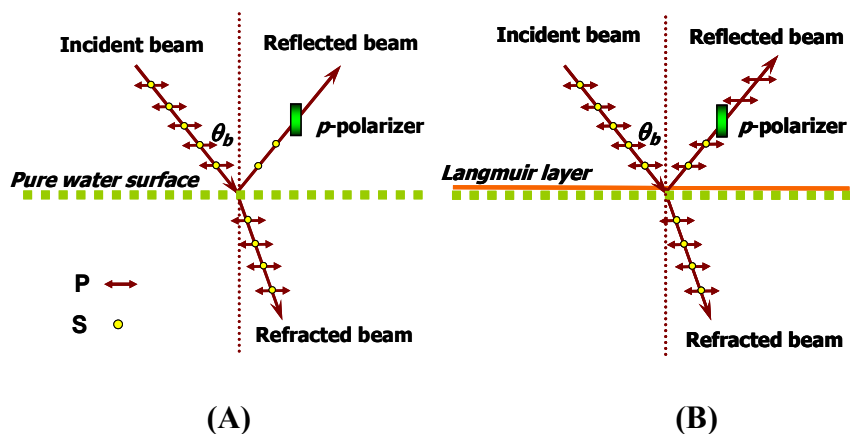
thesis.[25, 26]

**Figure 2.25.** Laser beam diagrams for Brewster angle microscopy: (A) a pure water surface and (B) a film covered surface. Arrows in the beams indicate radiation polarized in the p direction (in the plane of the paper). The radiation polarized in the s direction (open circles) is perpendicular (out of the plane of the paper) to the plane of incidence. The incident light is set to Brewster's angle ($\theta_b$) for pure water. A p-polarizer is placed in the path of the reflected beam to filter out the residual s component before it can reach the detector.


## 2.6. Brewster Angle Microscopy (BAM)

In this thesis, Brewster angle microscopy (BAM) is used to visualize the nucleation and growth of PCL crystals in Langmuir monolayers at the A/W interface. BAM is a noninvasive optical microscopy suitable for monitoring domain formation and growth during phase transitions in Langmuir films. Furthermore, BAM is capable of providing valuable information about the texture, size, homogeneity and other *in situ* morphological details of Langmuir films.[37, 38] A beam diagram for a BAM instrument using a polarized light source is shown in Figure 2.25. When light passes through a medium with a lower

refractive index into a medium with a higher refractive index, some fraction of p-polarized light will be reflected at all angles of incidence except at Brewster's angle ($\theta_B$).

In the experimental set-up of the Mini-BAM instrument, the angle of the incident light is set to Brewster's angle ($\theta_B$=53.1$^\circ$ for water) for the A/W interface, which minimizes the reflection of p-polarized light from a pure water surface as shown in Figure 2.25A. However, when a film resides at the A/W interface, the refractive index and thickness of the film will lead to a detectable reflectance of light at the interface as seen in Figure 2.25B. Detection of the reflected light with a position sensitive sensor like a charge coupled device (CCD) camera allows for visualization of the film's morphology.[37, 38]

The observation of domain morphologies in Langmuir films arises from differences in refractive index or thickness between different phases such as the gas, the liquid-expanded, liquid-condensed, and solid phases. According to Fresnel's laws, the reflectivity (R) of light from a surface depends on the angle and the polarization of incident light. For an ideal isotropic surface without roughness possessing an abrupt change in refractive index, the reflectivity of s-polarized light ($R_s$) is given by

$$R_s = \left( \frac{n_i \cos\theta_i - n_r \cos\theta_r}{n_i \cos\theta_r + n_r \cos\theta_i} \right)^2 = \frac{\sin^2(\theta_r - \theta_i)}{\sin^2(\theta_r + \theta_i)} \tag{2-50}$$

where $n_1$ (incident) and $n_2$ are the refractive indices of the two media, and $\theta_i$ and $\theta_r$ are the incident and refracted angles, respectively. The reflectivity of p-polarized light ($R_p$) is governed by Eq. 2-51:

$$R_p = \left( \frac{n_r \cos\theta_i - n_i \cos\theta_r}{n_i \cos\theta_r + n_r \cos\theta_i} \right)^2 = \frac{\tan^2(\theta_i - \theta_r)}{\tan^2(\theta_r + \theta_i)} \tag{2-51}$$

Both Eqs. 2-50 and 2-51 indicate that the reflectivity is dependent upon $\theta_i$ and $\theta_r$.

Additionally $\theta_i$ and $\theta_r$ are correlated through Snell's law:

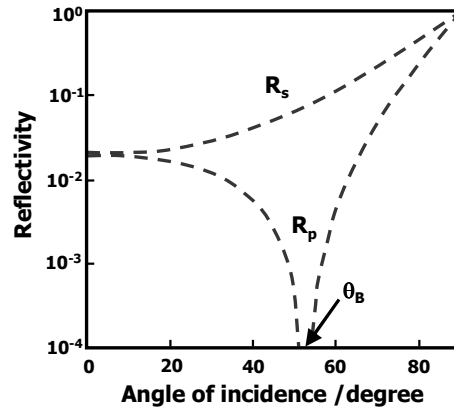$$n_i \sin \theta_i = n_r \sin \theta_r \tag{2-52}$$

**Figure 2.26.** Reflectivity vs. the angle of incidence. At Brewster's angle ($\theta_B = 53.1^\circ$ for the A/W interface), $R_p$ approaches zero.

The most important feature of Eqs. 2-50 and 2-51 with respect to BAM is the difference between $R_s$ and $R_p$ with respect to $\theta_i$. Figure 2.26 shows $R_s$ and $R_p$ as a function of $\theta_i$. As seen in Figure 2.26, $R_s$ shows a finite reflectivity at all $\theta_i$. In contrast, $R_p$ shows a sharp minimum as the incident angle increases and approaches zero when $\theta_i + \theta_t = 90^\circ$ resulting in $\tan(\theta_i + \theta_t) \to \infty$. $\theta_i$ at this point corresponds to Brewster's angle ($\theta_B$). According to Brewster's law ($\theta_i + \theta_t = 90^\circ$), Snell's law (Eq. 2-52) can be used to define Brewster's angle:

$$\tan \theta_B = n_2 / n_1 \tag{2-53}$$

Hence, a small shift in $\theta_B$ accompanying a change in film thickness or refractive index at the A/W interface causes $R_p$ to change significantly. For a thin film at the air (refractive index, $n_1$)/water (refractive index, $n_2$) interface with a refractive index profile, $n(z)$, the ellipticity, $\overline{\rho_B}$, at Brewster's angle is given by[37, 38]

$$\overline{\rho_B} = \frac{\pi}{\lambda} \frac{\sqrt{n_1^2 + n_2^2}}{n_1^2 - n_2^2} \int_{-\infty}^{+\infty} \frac{[n(z)^2 - n_1^2][n(z)^2 - n_2^2]}{n(z)^2} dz \qquad (2\text{-}54)$$

where z is the distance from the average interfacial position, z = 0. For an interfacial layer with a small interfacial width, D, which is small compared to the wavelength of the incident light, $\lambda$, Eq. 2-54 can be used to calculate the reflectivity of p-polarized light at Brewster's angle, $R_p(\theta_B)$:

$$R_p(\theta_B) \cong R_s(\theta_B)\overline{\rho_B}^2 \qquad (2\text{-}55)$$

where $R_s(\theta_B)$ is the reflectivity of s-polarized light at Brewster's angle from a Fresnel interface.[135] The validity of Eq. 2-55 arises from the fact that unlike $R_p$, $R_s$ does not change significantly for small changes in $\theta_B$ as one might expect from Figure 2.26. Thus, Eq. 2-55 can also be used estimate the dependence of the intensity of reflected light, $I_r$, from $\overline{\rho_B}$ for a given incident intensity, $I_i$:

$$I_r = I_i R_p(\theta) \propto \overline{\rho_B}^2 \qquad (2\text{-}56)$$

For films of uniform thickness, h, and a uniform refractive index, n, Eq. 2-56 can be written as

$$I_r = I_i R_p(\theta_B) \propto \overline{\rho_B}^2 = \left( \frac{\pi h}{\lambda_0} \frac{\sqrt{n_1^2 + n_2^2}}{n_1^2 - n_2^2} \frac{[n^2 - n_1^2][n^2 - n_2^2]}{n^2} \right)^2 \qquad (2\text{-}57)$$

where h is the thickness of the film.  Eq. 2-57 allows one to draw several conclusions.

First, during phase transitions in Langmuir films, both the refractive index and thickness

differences for different phases can lead to different $\overline{\rho_B}$ , hence, different $I_r$.  Thus, the

phase with higher $\overline{\rho_B}$ appears brighter and the phase with smaller $\overline{\rho_B}$  appears lighter in

BAM images.  Second, the reflected intensity in BAM studies is proportional to $h^2$.

Hence, BAM is more sensitive to thickness changes than changes in refractive index

normally accompanying phase transitions in Langmuir films at the A/W interface.

Finally, the surface roughness of Langmuir films caused by thermal fluctuations is

usually negligible because of the small amplitude for capillary waves on liquid surfaces

covered with monomolecular films relative to h.[136]

Figure 2.27 is a schematic diagram of the experimental set-up of the Mini-BAM

instrument which consists of a p-polarized diode laser source, a p-polarizer, a CCD

camera, and a Teflon trough. The only difference between the Mini-BAM and a

traditional BAM is the position of the polarizer. In Mini-BAM, the *p*-polarizer is placed

in the path of the reflected beam to filter out any residual *s* component before it reaches

the detector. In traditional BAM, the polarizer is in the path of the incident beam to

polarize most of the radiation in the *p* direction by removing the *s* component before it

reaches the surface. This feature enhances imaging resolution of the Mini-BAM.

Morphology studies using BAM can reveal information about domain structures,

molecular orientation, phase behavior, and other aggregation behavior as a function of

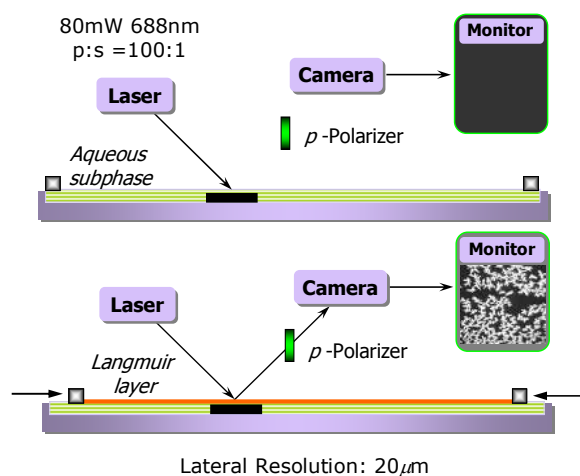surface concentration, temperature, and different type of subphases.

80mW 688nm
p:s =100:1

**Figure 2.27.** Schematic diagrams of Brewster angle microscopy at the A/W interface: a pure water surface (top) and a film covered surface (bottom). The Mini-BAM instrument consists of a *p*-polarized diode laser source (688 nm), a *p*-polarizer, a CCD camera, and a Teflon trough.

## 2.7. Atomic Force Microscopy (AFM)

Force microscopy methods first emerged in 1986 when Binnig and Gerber measured the forces between a small tip and an insulator surface.[137]  This newly invented technique developed quickly after the first silicon micro-cantilever was fabricated by Albrecht.[138] After several years' additional technical improvements,[139-142] atomic force microscopy (AFM) become a key tool for surface characterization in various research areas.  The atomic force microscope is widely used to map the morphology of surfaces (height image) and material properties such as surface hardness (phase image).  Moreover, AFM has emerged as the dominant techniques for measuring long range attractive or repulsive forces between a probe tip and sample surface (force curve measurements) in soft material systems.[143, 144]
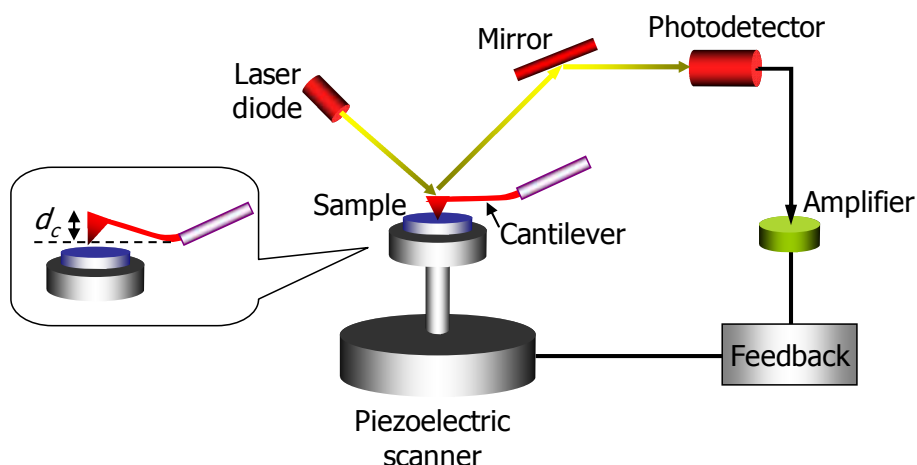
**Figure 2.28.** Schematic diagram of the experimental set-up for AFM.

Forces between a tip and a sample surface are too small ($< 10^{-9}$ N) to be measured directly. The simplified experimental set-up used in most AFM studies is illustrated in Figure 2.28. AFM tips are normally made from silicon or silicon nitride and attached to one end of a cantilever. A piezo-electric scanner is used to control tip-surface interactions in either constant force mode to gain height information, or constant height mode to gain force information, during the scanning process. A beam from a laser diode is focused onto the back of a reflective cantilever and the position of the cantilever is determined from where the reflected light strikes a position-sensitive photodetector. Normally, two photodiodes in the detector are used to accurately determine the position of the laser spot on the photodetector by measuring the difference in light intensities between the upper and lower photodetectors. Small motion of the tip will cause a small deflection of the cantilever. Thus, the reflected beam will be tilted, leading to a position change of the reflected laser beam on the position-sensitive photodetector. This signal is converted to a voltage. This optical method significantly magnifies the motion of the tip

because the beam distance from cantilever to detector is usually thousands of times greater than the length of the cantilever. To efficiently measure the small angular deflection of the cantilever, the cantilevers need to be highly flexible. The spring constant of typical AFM cantilevers is about 0.1 N/m.
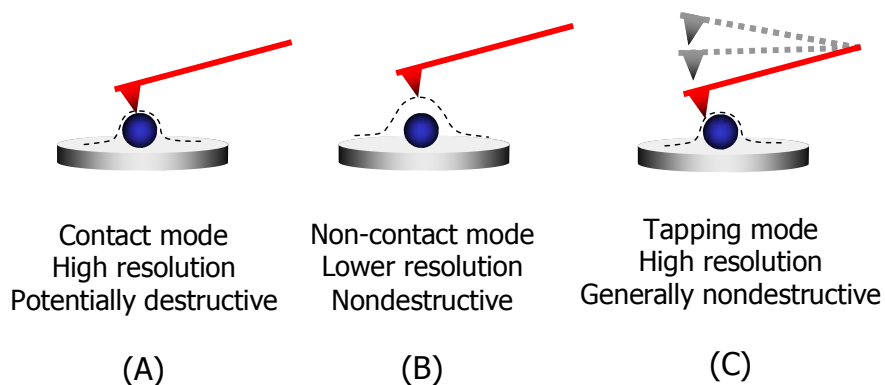
Contact mode
High resolution
Potentially destructive

(A)

Non-contact mode
Lower resolution
Nondestructive

(B)

Tapping mode
High resolution
Generally nondestructive

(C)

**Figure 2.29.** AFM operation modes. (A) contact mode, (B) non-contact mode; and (C) tapping mode.

According to sample surface properties, AFM can be operated in contact, non-contact and tapping modes. The classification of operation mode is based on the sample-tip interactions. In the contact mode, the tip scans the sample by closely contacting with the sample surface as depicted in Figure 2.29A. The deflection of the cantilever is detected and maintained at a constant value by adjusting the position of the sample relative to the cantilever. AFM operated in contact mode measures the height of objects on the surface and the lateral position of objects. In comparison with contact mode, a 50-150 Å gap is maintained between the tip and sample surface to avoid damaging the sample as seen in Figure 2.29B for non-contact mode. Attractive van der Waals forces acting between the tip and the sample are used to map the topography of the surface during the scanning

process. However, it is difficult to obtain high resolution images by non-contact mode because the measured attractive force is weaker than the repulsive force measured in contact mode.

Tapping mode AFM is most commonly used mode for characterizing polymeric materials. This operation mode allows the mapping of sample surfaces with higher resolution than non-contact mode and generally does less damage to the sample than contact mode. The cantilever alternatively places the tip on the surface to gain high resolution and lifts it off the surface to avoid dragging the tip on the surface as shown in Figure2.29c. The oscillation of the cantilever is controlled by a piezoelectric driver and is usually close to its own resonant frequency ~ 50,000 to 500,000 Hertz with an amplitude ranging from 20 to 100 nm. The amplitude of the cantilever is reduced when the oscillating tip approaches the surface. A feedback loop is used to keep the cantilever oscillating at a constant amplitude and to map the surface topography by the feedback of the amplitude signal. In addition, the phase lag of the cantilever oscillation relative to the signal sent to the piezoelectric driver can be simultaneously measured, which provides a phase image to characterize the components of composite materials based on material properties such as adhesion and hardness. Although the oscillating tip vertically contacts the sample surface during measurements, the high frequency can overcome sample-tip interactions, minimizing damage of the sample. Thus, tapping mode AFM is often regarded as a nondestructive characterization technique and has been widely used for characterizing the surface topography of soft materials such as polymers and biomaterials.